

Nonlinear projection-based model order reduction with machine learning regression for closure error modeling in the latent space

S. Ares de Parga^{b,c,*}, Radek Tezaur^a, Carlos G. Hernández^a, Charbel Farhat^{a,d}

^a*Department of Aeronautics and Astronautics, Stanford University, Stanford, CA 94305, USA*

^b*Department of Civil and Environmental Engineering, Universitat Politècnica de Catalunya - Barcelona Tech (UPC), Building B0, Campus Nord, Jordi Girona 1-3, Barcelona 08034, Spain*

^c*Centre Internacional de Mètodes Numèrics en Enginyeria (CIMNE), Universitat Politècnica de Catalunya, Building C1, Campus Nord, Jordi Girona 1-3, Barcelona 08034, Spain*

^d*Institute for Computational and Mathematical Engineering, Stanford University, Stanford, CA 94305, USA*

Abstract

A significant advancement in nonlinear projection-based model order reduction (PMOR) is presented through a highly effective methodology. This methodology employs Gaussian process regression (GPR) and radial basis function (RBF) interpolation for closure error modeling in the latent space, offering notable gains in efficiency and expanding the scope of PMOR. Moving beyond the limitations of deep artificial neural networks (ANNs), previously used for this task, this approach provides crucial advantages in terms of interpretability and a reduced demand for extensive training data. The capabilities of GPR and RBFs are showcased in two demanding applications: a two-dimensional parametric inviscid Burgers problem, featuring propagating shocks across the entire computational domain, and a complex three-dimensional turbulent flow simulation around an Ahmed body. The results demonstrate that this innovative approach preserves accuracy and achieves substantial improvements in efficiency and interpretability when contrasted with traditional PMOR and ANN-based closure modeling.

1. Introduction

The parametric numerical simulation of intricate physical phenomena, often relying on high-dimensional computational models (HDMs) based on partial differential equations, poses a significant bottleneck across various scientific and engineering disciplines. Projection-based Model Order Reduction (PMOR) [1] offers a compelling strategy to alleviate this computational burden by constructing low-dimensional surrogate models that faithfully approximate the dynamics of the original system at a fraction of the computational cost. Fundamentally, PMOR can be interpreted as a form of physics-based machine learning, where prior knowledge of the governing equations is leveraged to define a structured low-dimensional representation of the system's state space.

The field of PMOR has witnessed rapid advancements, particularly in addressing the limitations imposed by the Kolmogorov n -width barrier [2], which often restricts the efficiency of linear subspace methods for nonlinear systems. To overcome this, the advent of nonlinear PMOR techniques has been crucial. Unlike linear methods that approximate solutions within a fixed linear subspace, nonlinear PMOR allows the reduced-order approximation to lie on a nonlinear manifold or to be constructed through nonlinear mappings of the low-dimensional state. This capability enables them to capture more complex solution structures and the intrinsic nonlinearities of the underlying physics with greater efficiency than linear or affine counterparts, thus extending the applicability of PMOR to a wider range of complex parametric problems. Documented successes in fields like structural dynamics [3] and computational fluid dynamics (CFD) [4] highlight the significant potential of recent nonlinear PMOR methods to deliver accurate and efficient surrogate models for demanding scientific computing applications.

*Corresponding author – This paper was written during the author's residency at Stanford University
Email address: sebastian.ares@upc.edu (S. Ares de Parga)

The landscape of nonlinear PMOR is diverse, featuring various methodologies that offer distinct strengths and weaknesses. Some alternative approaches worth considering include:

- *Piecewise affine approximations.* These methods address nonlinearities by locally modeling systems with affine representations [5, 6]. A decade ago, they demonstrated real-time operation on a laptop for steady Reynolds-averaged Navier-Stokes (RANS) computations relevant to the NASA Common Research Model (CRM) [7]. Specifically, when combined with the least-squares Petrov-Galerkin (LSPG) PMOR method [8, 9] and the Gauss-Newton method with approximated tensors (GNAT) for hyperreduction [8], this approach successfully managed a parametric HDM with over $N = 6.8 \times 10^7$ dimensions for the RANS-based analysis of flow past the CRM. This was achieved at a Reynolds number of $Re = 5 \times 10^6$ in the transonic regime, in the presence of shocks, and across a shape parameter domain \mathcal{D} of dimension $N_{\mathcal{D}} = 4$ [10]. Recently, using the energy conserving sampling and weighting (ECSW) method for hyperreduction [6], it significantly accelerated the detached eddy simulations (DES) of unsteady turbulent flow around an F-16 C/D Block 40 fighter jet at 10 000 feet with a 30° angle of attack and a free-stream Mach number $M_\infty = 0.3$ ($Re = 1.82 \times 10^7$). This resulted in reductions of wall-clock time by three orders of magnitude and CPU time by five orders, while maintaining 98% accuracy [6]. However, as $N_{\mathcal{D}}$ increases, this approach may face performance challenges due to the Kolmogorov barrier. For second-order dynamical systems, it may encounter challenges related to global smoothness; however, these challenges are manageable.
- *Registration methods.* These methods specifically target the Kolmogorov n -width issue, particularly in transport problems. They transform the traditional affine subspace approximation into a nonlinear form through nonlinear parameterization [11, 12]. This process involves mesh motion and deformation within the semi-discrete or discrete HDM. Recent applications include transonic inviscid steady flow past airfoils, parameterized by their upper and lower thicknesses, free-stream Mach number, and angle of attack [13]. They have also been applied to hypersonic viscous steady flow over a cylinder, parameterized by the Mach number [14]. Nevertheless, applying these methods robustly to complex three-dimensional (3D) geometries, particularly in CFD problems with large-scale meshes at high Reynolds numbers, can present significant challenges. Their feasibility for time-dependent computations, such as unsteady flow simulations with long-distance traveling features, also requires further investigation.
- *Quadratic approximation manifolds.* To overcome the Kolmogorov barrier, quadratic approximation manifolds have been proposed in two forms: a simulation-free version for structural dynamics [15] and a more general, computationally efficient data-driven version demonstrated for convection-dominated turbulent flows and other transport problems [16]. Furthermore, quadratic solution approximations have been developed for nonintrusive ¹ PMOR via operator inference [17].

Notably, the quadratic approximation manifold from [16] was successfully integrated with the LSPG PMOR method [8, 9] and the ECSW hyperreduction technique. This integration demonstrated its effectiveness in addressing the Ahmed body turbulent wake flow problem – a well-known CFD benchmark in the automotive industry – where time was the sole parameter. The combined approach significantly accelerated the HDM, achieving a reduction of two orders of magnitude in wall-clock time and three in CPU time, while maintaining accuracy above 97%. Compared to traditional PMOR with affine approximation and ECSW hyperreduction, the quadratic approximation method reduced the online wall clock time for integrated and probe aerodynamic quantities by more than 32-fold [16].

In [4], this combined approach also demonstrated superiority over the integration of the traditional affine approximation with LSPG and ECSW for a 3D benchmark steady hypersonic flow problem parameterized by the free-stream Mach number. It accelerated the underlying HDM, which had a dimension of $N = 654\,720$, by a factor of 291 and reduced its CPU time by a factor of 41 920 while maintaining the desired levels of accuracy and fidelity – factors that, for this relatively small scale problem, are higher than those associated with the traditional affine approximation.

¹A nonintrusive model reduction method is a low-dimensional approximation constructed offline from solution snapshots of a discretized partial differential equation (PDE), without online dependence on or modification of the discretized PDE.

- *Framework for PMOR via latent space closure error modeling.* Developed within the context of the LSPG PMOR method in [18] and mathematically analyzed in [19], this framework enables the creation of an arbitrarily nonlinear approximation manifold by modeling the closure error associated with the traditional affine approximation in its latent space using a deep artificial neural network (ANN). Unlike previous methods that employed various forms of ANNs for model reduction, the training of a projection-based reduced-order model (PROM) constructed using this framework and referred to as a PROM-ANN, does not require an amount of data that scales with the dimension of the HDM. Consequently, this framework stands out as the only intrusive ANN-based or ANN-incorporating model reduction approach successfully demonstrated for problems with over 21 000 dimensions and is among the few such frameworks amenable to hyperreduction. For a parametric, unsteady, shock-dominated benchmark problem exhibiting the Kolmogorov n -width issue and an HDM dimension of $N = 1\,125\,000$, the PROM constructed using this framework – hyperreduced via ECSW and dubbed HPROM-ANN – achieved superior accuracy compared to a traditional HPROM based on an affine approximation of dimension $n = 95$. This was accomplished with an almost order-of-magnitude smaller dimension, executing online approximately 70 times faster. Notably, the HPROM-ANN with a dimension of $n = 10$ accelerated the HDM by nearly three orders of magnitude while maintaining a 97% accuracy level.

Furthermore, in [4], this framework was successfully applied to reduce HDMs based on the Navier-Stokes equations in the hypersonic flow regime. It facilitated the construction of an HPROM-ANN for a version of the 3D double-cone steady benchmark problem in hypersonic CFD, parameterized by the free-stream Mach number. This approach achieved a dimension as small as $n = 2$ and accelerated the underlying HDM, which has a dimension of $N = 654\,720$, by more than three orders of magnitude. Additionally, it reduced CPU time by over five orders of magnitude while maintaining the desired levels of accuracy and fidelity.

However, this framework for nonlinear PMOR has certain limitations as well, which are outlined below and addressed in this paper.

The nonlinear PMOR framework introduced in [18] offers substantial advantages by addressing closure errors from an affine approximation within the latent space. By directly tackling these errors in the reduced-order space, it circumvents the need for costly high-dimensional reconstructions often required by other machine learning-enhanced model order reduction methods. Additionally, the application of deep ANNs effectively captures the complex nonlinear relationships inherent in closure terms, as evidenced by its documented successes [18, 19]. Building on these strengths, this paper seeks to further advance several aspects of the framework.

A key advantage of PMOR lies in its capacity to yield a priori error estimators, bounds, or indicators, offering crucial insights into the accuracy and reliability of the PROM [20, 21]. However, a significant limitation of the current PMOR framework employing latent space closure error modeling is the inherent lack of interpretability within the deep ANN used for regression. This opacity impedes the development of rigorous theoretical a priori error estimates or indicators for the approach. Addressing this non-interpretability served as the primary motivation for the research presented herein. Furthermore, when applied to parametric problems with a small parameter domain dimension $N_{\mathcal{D}}$, traditional PMOR based on affine approximation necessitates a relatively modest number of solution snapshots, potentially leading this framework to an HPROM-ANN with exceptionally low dimensionality. This dimensionality often closely aligns with the intrinsic dimension of the solution manifold, particularly when the solution’s dependence on parameters is simple and low-dimensional, such as linear variation with each parameter independently. As discussed in Section 3.1, such scenarios tend to provide insufficient data for effective deep ANN training to model the closure error associated with the traditional affine approximation in its latent space, thus necessitating a complementary strategy to generate additional training data beyond the initial high-dimensional solution snapshots for constructing the desired, extremely low-dimensional HPROM-ANN.

To address these limitations and lay the groundwork for more robust, theoretically grounded nonlinear PROMs based on the aforementioned framework for nonlinear PMOR, this paper introduces a less data-intensive regression approach that employs interpretable machine learning techniques to model closure error within the latent space. Specifically, its main contribution is a generalized framework for creating HPROMs that incorporate latent-space closure error modeling, utilizing two closely related interpretable regression methods: standard Gaussian process regression (GPR) and radial basis function (RBF) interpolation. These

techniques not only provide valuable insights into the structure of the closure error, thereby addressing the first limitation of non-interpretability and paving the way for a priori error estimates, but also require significantly less training data compared to more complex regression methods such as deep ANNs and therefore are more appropriate for addressing the second limitation: the scarcity of training data when a very small value of n can be achieved for a given level of accuracy.

The resulting computational framework is demonstrated within the established methodologies of the LSPG method for constructing PROMs and the ECSW method for transforming them into computationally efficient HPROMs. While these methods provide the operational context for showcasing the framework’s utility, only the essential elements needed for their use in the present nonlinear PROM setting are overviewed. The detailed derivations follow the comprehensive treatment in [18], which addresses the modeling of closure error associated with the traditional affine approximation through a deep ANN within its latent space. It should be emphasized, however, that the proposed framework is not limited to this setting and remains readily applicable to Galerkin projection and to alternative hyperreduction techniques beyond ECSW.

The remainder of this paper is structured as follows. Section 2 reviews the foundational framework for PMOR via latent space closure error modeling and details its incorporation within the LSPG projection and ECSW hyperreduction methods, establishing the notation and nomenclature used throughout the paper. Section 3 begins with a concise overview of modeling the closure error inherent in the traditional affine approximation using deep ANNs and pre-computed solution snapshots. It then argues for GPR and RBF interpolation as more effective alternatives for closure error modeling. Section 4 presents two applications to showcase these alternatives and demonstrate their advantages. The first, a readily reproducible two-dimensional (2D) parametric inviscid Burgers problem features shocks propagating across the domain, posing a significant challenge for both traditional PMOR and many nonlinear PMOR techniques, including registration methods. The second application is a benchmark CFD problem from the automotive industry, simulating turbulent flow over a generic bluff body representative of a simplified car using the DES turbulence model. Section 5 concludes that GPR and RBF-based closure error modeling in PMOR significantly extends the reach of nonlinear PMOR, offering better efficiency, accuracy, and interpretability, and effectively tackling the Kolmogorov barrier in complex flows.

2. Projection-based model order reduction with closure error modeling in the latent space

Following the standard procedure for constructing a PROM, the nonlinear PMOR framework with latent space closure error modeling commences by collecting N_s solution snapshots \mathbf{u}^s ($s = 1, \dots, N_s$) into a snapshot matrix $\mathbf{S} \in \mathbb{R}^{N \times N_s}$. Here, N represents the dimension of the high-dimensional semi-discrete or discrete problem to be solved. Subsequently, this snapshot matrix \mathbf{S} is compressed using a thin singular value decomposition (SVD) based on a singular value energy truncation criterion.

Specifically, the thin SVD of the snapshot matrix yields $\mathbf{S} = \mathbf{U}_\mathbf{S} \mathbf{\Sigma}_\mathbf{S} \mathbf{Y}_\mathbf{S}^T$, where:

- $\mathbf{U}_\mathbf{S} \in \mathbb{R}^{N \times \min(N, N_s)}$ contains the left singular vectors, whose columns span the range of \mathbf{S} .
- $\mathbf{\Sigma}_\mathbf{S} \in \mathbb{R}^{k \times k}$ is a diagonal matrix holding the nonzero singular values $\sigma_{\mathbf{S},i}$ ($i \in \{1, \dots, k\}$) arranged in descending order: $\sigma_{\mathbf{S},1} \geq \sigma_{\mathbf{S},2} \geq \dots \sigma_{\mathbf{S},k} > 0$, where $k \leq \min(N, N_s)$.
- $\mathbf{Y}_\mathbf{S} \in \mathbb{R}^{N_s \times \min(N, N_s)}$ contains the right singular vectors, whose columns span the range of \mathbf{S}^T .
- k represents the rank of the snapshot matrix \mathbf{S} .
- The superscript T denotes the transpose operation.

Subsequently, an orthogonal reduced-order basis (ROB) matrix $\mathbf{V}_{\text{tot}} \in \mathbb{R}^{N \times n_{\text{tot}}}$ is formed by selecting the first $n_{\text{tot}} \ll N$ columns of the left singular vector matrix $\mathbf{U}_\mathbf{S}$ obtained from the thin SVD. The orthogonality of the columns is inherent to the left singular vectors, satisfying $\mathbf{V}_{\text{tot}}^T \mathbf{V}_{\text{tot}} = \mathbf{I}_{n_{\text{tot}}}$, where $\mathbf{I}_{n_{\text{tot}}}$ is the $n_{\text{tot}} \times n_{\text{tot}}$ identity matrix. The reduced dimension n_{tot} is typically determined by the singular value energy truncation criterion

$$1 - \frac{\sum_{i=1}^{n_{\text{tot}}} \sigma_{\mathbf{S},i}^2}{\sum_{j=1}^k \sigma_{\mathbf{S},j}^2} \leq \varepsilon_{\mathbf{S}}^2 \quad (1)$$

where $\varepsilon_{\mathbf{S}} > 0$ is a user-defined tolerance that controls the amount of energy captured by the reduced basis.

Then, this orthogonal basis \mathbf{V}_{tot} is partitioned into two submatrices, $\mathbf{V} \in \mathbb{R}^{N \times n}$ and $\bar{\mathbf{V}} \in \mathbb{R}^{N \times \bar{n}}$, such that $n \ll \bar{n} \ll N$ and $n + \bar{n} = n_{\text{tot}}$

$$\mathbf{V}_{\text{tot}} = [\mathbf{V} \quad \bar{\mathbf{V}}] \quad (2)$$

Given the orthogonality of the reduced-order basis \mathbf{V}_{tot} , its partitioned submatrices \mathbf{V} and $\bar{\mathbf{V}}$ satisfy the following orthogonality conditions

$$\mathbf{V}^T \mathbf{V} = \mathbf{I}_n, \quad \bar{\mathbf{V}}^T \bar{\mathbf{V}} = \mathbf{I}_{\bar{n}}, \quad \text{and} \quad \mathbf{V}^T \bar{\mathbf{V}} = \mathbf{0}_{n \times \bar{n}} \quad (3)$$

Next, leveraging the reduced-order bases \mathbf{V} and $\bar{\mathbf{V}}$, the high-dimensional solution \mathbf{u} of the parametric and possibly time-dependent problem of interest is approximated as

$$\mathbf{u}(t; \boldsymbol{\mu}) \approx \tilde{\mathbf{u}}(t; \boldsymbol{\mu}) = \mathbf{u}_{\text{ref}} + \mathbf{V}\mathbf{q}(t; \boldsymbol{\mu}) + \bar{\mathbf{V}}\bar{\mathbf{q}}(t; \boldsymbol{\mu}) \quad (4)$$

In this reduced-order approximation, t denotes time, $\boldsymbol{\mu} \in \mathcal{D} \subseteq \mathbb{R}^{N_{\mathcal{D}}}$ represents the parameter vector, and \mathbf{u}_{ref} is a reference solution. Furthermore, $\mathbf{q} \in \mathbb{R}^n$ and $\bar{\mathbf{q}} \in \mathbb{R}^{\bar{n}}$ are the vectors of generalized coordinates corresponding to the ROBs \mathbf{V} and $\bar{\mathbf{V}}$, respectively.

Using the partitioned basis from (2), the solution approximation (4) can be compactly expressed as

$$\tilde{\mathbf{u}}(t; \boldsymbol{\mu}) = \mathbf{u}_{\text{ref}} + [\mathbf{V} \quad \bar{\mathbf{V}}] \begin{bmatrix} \mathbf{q}(t; \boldsymbol{\mu}) \\ \bar{\mathbf{q}}(t; \boldsymbol{\mu}) \end{bmatrix} = \mathbf{V}_{\text{tot}} \mathbf{q}_{\text{tot}}(t; \boldsymbol{\mu}) \quad (5)$$

This compact form motivates the following considerations for choosing the dimensions of the partitioned bases:

- Set the total reduced dimension n_{tot} to be equal to n_{tra} . This n_{tra} value is calculated using (1) within a traditional affine subspace approximation, as shown in (5), ensuring the desired accuracy is met regardless of the resulting computational cost.
- Select the dimension n of the *primary* basis \mathbf{V} to be minimal, ideally aligning with the intrinsic dimension of the solution manifold. This dimension often closely corresponds to the dimension $N_{\mathcal{D}}$ of the parameter domain \mathcal{D} when the mapping from \mathcal{D} to the solution manifold behaves like a low-dimensional embedding, preserving essential information without significant added complexity.
- Determine the dimension of the *secondary* basis as $\bar{n} = n_{\text{tra}} - n$.
- Using the pre-computed solution snapshots, learn *offline* the relationship between the generalized coordinates in $\bar{\mathbf{q}}(t; \boldsymbol{\mu})$ and their counterparts in $\mathbf{q}(t; \boldsymbol{\mu})$ through a map $\mathcal{N} : \mathbb{R}^n \rightarrow \mathbb{R}^{\bar{n}}$ (see Section (3.1)) such that

$$\bar{\mathbf{q}}(t; \boldsymbol{\mu}) = \mathcal{N}(\mathbf{q}(t; \boldsymbol{\mu})) \quad (6)$$

This allows rewriting the solution approximation (5) as

$$\tilde{\mathbf{u}}(t; \boldsymbol{\mu}) = \mathbf{u}_{\text{ref}} + \mathbf{V}\mathbf{q}(t; \boldsymbol{\mu}) + \bar{\mathbf{V}}\mathcal{N}(\mathbf{q}(t; \boldsymbol{\mu})) \quad (7)$$

and demonstrates that the resulting PROM will have a dimension $n = n_{\text{tra}} - \bar{n} \ll n_{\text{tra}}$. Consequently, throughout the remainder of this paper, the columns of the primary ROB $\mathbf{V} \in \mathbb{R}^{N \times n}$ will be referred to as the *retained modes*, and those of the ROB $\bar{\mathbf{V}}$ will be referred to as the *discarded modes*, where “discarded” emphasizes that the columns of $\bar{\mathbf{V}}$ do not directly contribute to the dimension of the PROM but do contribute to the embedded information. Similarly, \mathbf{q} will be referred to as the vector of *primary generalized coordinates* and $\bar{\mathbf{q}}$ as the vector of *secondary generalized coordinates*.

Note that in the approximation (7), the term $\bar{\mathbf{V}}\mathcal{N}(\mathbf{q})$ can be interpreted in four distinct ways:

- *Closure error modeling*: It serves as a data-driven model for the closure error, representing the difference between the full approximation and its affine part $\mathbf{u}_{\text{ref}} + \mathbf{V}\mathbf{q}(t; \boldsymbol{\mu})$.

- *Variational multiscale method*: It represents a variational multiscale approach, where the affine approximation captures the coarser scales of the solution and the correction term accounts for the finer scales.
- *Nonlinear ROB/PROM compression*: It signifies a nonlinear compression of a higher-dimensional ROB and its associated PROM down to a lower dimension $n \ll n_{\text{tra}}$.
- *Efficient snapshot utilization*: It represents a most efficient utilization of a set of solution snapshots that define a solution manifold parameterized by $(\mathbf{q}; \bar{\mathbf{q}} = \mathcal{N}(\mathbf{q}))$.

Furthermore, the solution approximation (7) represents a nonlinear approximation precisely because the map \mathcal{N} inherently introduces nonlinearity as it transforms the primary generalized coordinates $\mathbf{q} \in \mathbb{R}^n$ to the secondary generalized coordinates $\bar{\mathbf{q}} \in \mathbb{R}^{\bar{n}}$. Consequently, for complex nonlinear problems, this approach offers a significant advantage over traditional affine approximations.

The temptation might arise to think that by substituting a relationship like (6) (which defines $\bar{\mathbf{q}}$ in terms of \mathbf{q}) into (4), the resulting solution approximation, residing within the span of the ROB \mathbf{V}_{tot} of a traditional affine approximation with dimension $n_{\text{tot}} = n_{\text{tra}}$, might not be effective in overcoming the Kolmogorov barrier. However, this intuition is misleading. The nonlinear approximation (7) achieves a crucial advantage: it delivers a solution nearly identical to that of a traditional affine approximation while requiring only a small fraction of the latter’s dimensionality. In essence, the nonlinear approximation (7) significantly *delays* the onset of the limitations imposed by the Kolmogorov barrier.

It may be also tempting to interpret the closure error modeling discussed in this paper as yet another attempt to model the influence of unresolved modes on the evolution of resolved ones – a common practice in turbulence models or the PMOR of dynamical systems that incorporate turbulence modeling. While the approach discussed in this paper can be interpreted in this way, it was neither specifically designed for, nor is it limited to, such applications. In those contexts, “modes” typically refer to Fourier modes, which are intrinsically linked to spatial or frequency resolution. In contrast, our paper uses proper orthogonal decomposition (POD) modes, where the concept of “resolution” is fundamentally different. While Fourier resolution is defined by spatial or frequency scales, POD resolution relates to the dimensionality and accuracy of the model’s modal representation.

2.1. Least-squares Petrov-Galerkin projection

Given the generic, parametric, nonlinear, semi-discrete, first-order initial value problem

$$\mathbf{M}(\boldsymbol{\mu}) \dot{\mathbf{u}}(t; \boldsymbol{\mu}) + \mathbf{f}(\mathbf{u}(t; \boldsymbol{\mu}); \boldsymbol{\mu}) - \mathbf{g}(t; \boldsymbol{\mu}) = \mathbf{0}, \quad \mathbf{u}(0; \boldsymbol{\mu}) = \mathbf{u}^0(\boldsymbol{\mu}) \quad (8)$$

the dimensionality of this HDM is reduced via LSPG projection. This procedure follows the exact formulation introduced in [8, 9] and is directly applicable to the nonlinear approximations considered herein. For completeness and clarity, the essential elements of the LSPG projection are recalled below. Comprehensive derivations and implementation details for incorporating a solution approximation that features latent-space closure error modeling into the LSPG framework are provided in [18]

Employing the nonlinear approximation

$$\tilde{\mathbf{u}}(t; \boldsymbol{\mu}) = \mathbf{u}_{\text{ref}} + \mathbf{V} \mathbf{q}(t; \boldsymbol{\mu}) + \bar{\mathbf{V}} \mathcal{N}(\mathbf{q}(t; \boldsymbol{\mu})) \quad (9)$$

the associated residual of the HDM (8) is defined as

$$\mathbf{r}(\tilde{\mathbf{u}}(t; \boldsymbol{\mu}), t; \boldsymbol{\mu}) = \mathbf{M}(\boldsymbol{\mu}) \left(\mathbf{V} + \bar{\mathbf{V}} \frac{\partial \mathcal{N}}{\partial \mathbf{q}}(\mathbf{q}(t; \boldsymbol{\mu})) \right) \dot{\mathbf{q}}(t; \boldsymbol{\mu}) + \mathbf{f}(\tilde{\mathbf{u}}(t; \boldsymbol{\mu}); \boldsymbol{\mu}) - \mathbf{g}(t; \boldsymbol{\mu})$$

After an implicit time discretization, the time-discrete residual equation at step t^{m+1} is

$$\mathbf{r}^{m+1}(\boldsymbol{\mu}) = \mathbf{r}(\mathbf{u}_{\text{ref}} + \mathbf{V} \mathbf{q}^{m+1}(\boldsymbol{\mu}) + \bar{\mathbf{V}} \mathcal{N}(\mathbf{q}^{m+1}(\boldsymbol{\mu})), t^{m+1}; \boldsymbol{\mu}) = \mathbf{0} \quad (10)$$

where $\mathbf{r}^{m+1} \in \mathbb{R}^N$, and the superscript $m+1$ designates a discrete quantity evaluated at time t^{m+1} . This system is typically overdetermined as it governs $N \gg n$ unknowns. It is solved by enforcing the orthogonality

of the discrete residual to a suitable test space spanned by the ROB $\mathbf{W}^{m+1}(\boldsymbol{\mu}) \in \mathbb{R}^{N \times n}$, which yields the projected system

$$(\mathbf{W}^{m+1}(\boldsymbol{\mu}))^T \mathbf{r}(\mathbf{u}_{\text{ref}} + \mathbf{V} \mathbf{q}^{m+1}(\boldsymbol{\mu}) + \bar{\mathbf{V}} \mathcal{N}(\mathbf{q}^{m+1}(\boldsymbol{\mu}), t^{m+1}; \boldsymbol{\mu})) = \mathbf{0} \quad (11)$$

Within the LSPG method, this nonlinear system is typically solved using a Gauss-Newton iteration. Linearizing (11) at iteration k yields the linear update equation for $\Delta \mathbf{q}^{m+1, k+1}$

$$(\mathbf{W}^{m+1, k+1}(\boldsymbol{\mu}))^T \mathbf{W}^{m+1, k+1}(\boldsymbol{\mu}) \Delta \mathbf{q}^{m+1, k+1} = - (\mathbf{W}^{m+1, k+1}(\boldsymbol{\mu}))^T \mathbf{r}(\tilde{\mathbf{u}}(\mathbf{q}^{m+1, k}; \boldsymbol{\mu}), t^{m+1}; \boldsymbol{\mu}) \quad (12)$$

where the test basis $\mathbf{W}^{m+1, k+1}$ is explicitly given by

$$\mathbf{W}^{m+1, k+1}(\boldsymbol{\mu}) = \mathbf{J}^{m+1, k}(\boldsymbol{\mu}) \left[\mathbf{V} + \bar{\mathbf{V}} \frac{\partial \mathcal{N}}{\partial \mathbf{q}}(\mathbf{q}^{m+1, k}) \right] \quad (13)$$

and $\mathbf{J}^{m+1, k}(\boldsymbol{\mu}) := \frac{\partial \mathbf{r}}{\partial \tilde{\mathbf{u}}}(\tilde{\mathbf{u}}(\mathbf{q}^{m+1, k}), t^{m+1}; \boldsymbol{\mu})$ is the residual Jacobian with respect to the state. This formulation remains valid for any differentiable nonlinear map \mathcal{N} .

Based on the definition in (13), solving the discrete PROM problem (11) is equivalent to solving the nonlinear least-squares optimization problem

$$\mathbf{q}^{m+1}(\boldsymbol{\mu}) = \arg \min_{\mathbf{x} \in \mathbb{R}^n} \left\| \mathbf{r}(\mathbf{u}_{\text{ref}} + \mathbf{V} \mathbf{x} + \bar{\mathbf{V}} \mathcal{N}(\mathbf{x}), t^{m+1}; \boldsymbol{\mu}) \right\|_2^2 \quad (14)$$

2.2. Energy-conserving sampling and weighting hyperreduction

For nonlinear PROMs derived from LSPG projection, the computational complexity of evaluating the high-dimensional residual and Jacobian typically scales with the HDM dimension N , not just with the reduced dimension n . This dependence on N can become a significant bottleneck in real-time or many-query settings. Hyperreduction techniques address this challenge by decoupling online computational costs from N . Among these, the ECSW method, originally developed for second-order dynamical systems [22, 23] and recently extended to first-order dynamical systems [6], has proven particularly effective and has been successfully adapted to PROMs with general closure error modeling in the latent space [18]. The ECSW formulation is briefly summarized below in this generalized context, while full derivations and implementation details can be found in [23, 18].

Consider the set of mesh entities $\mathcal{E} = \{e_i\}_{i=1}^{N_e}$ defining the high-dimensional semi-discrete model. At each discrete time step t^{m+1} , the LSPG projection leads to the projected residual

$$\begin{aligned} \mathbf{r}_n^{m+1}(\boldsymbol{\mu}) &= (\mathbf{W}^{m+1}(\boldsymbol{\mu}))^T \mathbf{r}(\mathbf{u}_{\text{ref}} + \mathbf{V} \mathbf{q}^{m+1}(\boldsymbol{\mu}) + \bar{\mathbf{V}} \mathcal{N}(\mathbf{q}^{m+1}(\boldsymbol{\mu}), t^{m+1}; \boldsymbol{\mu})) \\ &= \sum_{e_i \in \mathcal{E}} (\mathbf{L}_{e_i} \mathbf{W}^{m+1}(\boldsymbol{\mu}))^T \mathbf{r}_{e_i}(\mathbf{L}_{e_i^+} [\mathbf{u}_{\text{ref}} + \mathbf{V} \mathbf{q}^{m+1}(\boldsymbol{\mu}) + \bar{\mathbf{V}} \mathcal{N}(\mathbf{q}^{m+1}(\boldsymbol{\mu}))], t^{m+1}; \boldsymbol{\mu}) \end{aligned} \quad (15)$$

Here, $\mathbf{r}_{e_i} \in \mathbb{R}^{d_{e_i}}$ denotes the local contribution of element e_i to the global residual, with d_{e_i} representing the number of attached degrees of freedom. The Boolean matrices $\mathbf{L}_{e_i} \in \{0, 1\}^{d_{e_i} \times N}$ and $\mathbf{L}_{e_i^+} \in \{0, 1\}^{d_{e_i^+} \times N}$ select the degrees of freedom associated with the mesh entity e_i and its neighboring elements within the numerical stencil, respectively.

ECSW approximates this residual using a sparse cubature rule with strictly positive weights $\xi_{e_i} > 0$ over a significantly reduced mesh $\tilde{\mathcal{E}} \subset \mathcal{E}$, giving

$$\tilde{\mathbf{r}}_n^{m+1}(\boldsymbol{\mu}) = \sum_{e_i \in \tilde{\mathcal{E}}} \xi_{e_i} (\mathbf{L}_{e_i} \mathbf{W}^{m+1}(\boldsymbol{\mu}))^T \mathbf{r}_{e_i}(\mathbf{L}_{e_i^+} [\mathbf{u}_{\text{ref}} + \mathbf{V} \mathbf{q}^{m+1}(\boldsymbol{\mu}) + \bar{\mathbf{V}} \mathcal{N}(\mathbf{q}^{m+1}(\boldsymbol{\mu}))], t^{m+1}; \boldsymbol{\mu}) \quad (16)$$

Similarly, the Jacobian of the projected residual is

$$\begin{aligned} \mathbf{J}_n^{m+1}(\boldsymbol{\mu}) &= (\mathbf{W}^{m+1}(\boldsymbol{\mu}))^T \mathbf{J}^{m+1}(\boldsymbol{\mu}) = (\mathbf{W}^{m+1}(\boldsymbol{\mu}))^T \frac{\partial \mathbf{r}^{m+1}}{\partial \tilde{\mathbf{u}}^{m+1}}(\mathbf{u}_{\text{ref}} + \mathbf{V}\mathbf{q}^{m+1}(\boldsymbol{\mu}) + \bar{\mathbf{V}}\mathcal{N}(\mathbf{q}^{m+1}(\boldsymbol{\mu})), t^{m+1}; \boldsymbol{\mu}) \\ &= \sum_{e_i \in \mathcal{E}} (\mathbf{L}_{e_i} \mathbf{W}^{m+1}(\boldsymbol{\mu}))^T \mathbf{J}_{e_i}(\mathbf{L}_{e_i}^+ [\mathbf{u}_{\text{ref}} + \mathbf{V}\mathbf{q}^{m+1}(\boldsymbol{\mu}) + \bar{\mathbf{V}}\mathcal{N}(\mathbf{q}^{m+1}(\boldsymbol{\mu}))], t^{m+1}; \boldsymbol{\mu}) \end{aligned}$$

where $\mathbf{J}_{e_i}(\cdot) \in \mathbb{R}^{d_{e_i} \times d_{e_i}}$ is the contribution of mesh entity e_i to the discrete Jacobian. Given that

$$(\mathbf{W}^{m+1}(\boldsymbol{\mu}))^T \frac{\partial \mathbf{r}^{m+1}}{\partial \tilde{\mathbf{u}}^{m+1}} = \frac{\partial \left((\mathbf{W}^{m+1}(\boldsymbol{\mu}))^T \mathbf{r}^{m+1} \right)}{\partial \tilde{\mathbf{u}}^{m+1}}$$

it follows that $\mathbf{J}_n^{m+1}(\boldsymbol{\mu})$ is the Jacobian of the projected residual in (15). Therefore, it can be approximated using the same ECSW cubature rule as in (16), namely

$$\mathbf{J}_n^{m+1}(\boldsymbol{\mu}) \approx \sum_{e_i \in \tilde{\mathcal{E}}} \xi_{e_i} (\mathbf{L}_{e_i} \mathbf{W}^{m+1}(\boldsymbol{\mu}))^T \mathbf{J}_{e_i}(\mathbf{L}_{e_i}^+ [\mathbf{u}_{\text{ref}} + \mathbf{V}\mathbf{q}^{m+1}(\boldsymbol{\mu}) + \bar{\mathbf{V}}\mathcal{N}(\mathbf{q}^{m+1}(\boldsymbol{\mu}))], t^{m+1}; \boldsymbol{\mu})$$

ECSW's offline training proceeds by determining a sparse vector of cubature weights $\boldsymbol{\xi}$ and the associated reduced mesh $\tilde{\mathcal{E}}$. This is achieved by solving a nonnegative least-squares problem that minimizes the difference between projected residual contributions collected in the training snapshot subset and their sparse approximation

$$\boldsymbol{\xi} = \arg \min_{\boldsymbol{\xi} \geq 0} \|\mathbf{C}\boldsymbol{\xi} - \mathbf{d}\|_2^2 \quad \text{s.t.} \quad \|\mathbf{C}\boldsymbol{\xi} - \mathbf{d}\|_2 \leq \varepsilon_{\text{ECSW}} \|\mathbf{d}\|_2 \quad (17)$$

where the matrix \mathbf{C} and vector \mathbf{d} encode the contributions of the individual mesh entities to the projected residual evaluated at the training snapshots. Each row of \mathbf{C} corresponds to a training snapshot and contains the element-wise projected residual evaluations, while each column corresponds to a mesh entity e_i . The vector \mathbf{d} stores the corresponding full projected residual for each snapshot, obtained by aggregating these element-wise contributions (see [23, 18] for full details).

The resulting ECSW approximation significantly reduces online computational complexity, scaling only with the reduced mesh size $|\tilde{\mathcal{E}}| \ll N_e$ and the PROM dimension n , rather than the original problem dimension N . For nonlinear approximations, an additional step is required during the ECSW training phase because the generalized coordinates \mathbf{q}^s associated with each high-dimensional snapshot \mathbf{u}^s cannot be computed by orthogonal projection and must instead be obtained by solving in a least-squares sense the nonlinear system of the form

$$\boldsymbol{\delta}(\mathbf{q}') = \mathbf{u}_{\text{ref}} + \mathbf{V}\mathbf{q}' + \bar{\mathbf{V}}\mathcal{N}(\mathbf{q}') - \mathbf{u}^s = \mathbf{0} \quad (18)$$

using a Gauss-Newton method with Moore-Penrose updates

$$\mathbf{q}'^{(0)} = \mathbf{V}^T(\mathbf{u}^s - \mathbf{u}_{\text{ref}}) \quad (19)$$

$$\mathbf{q}'^{(k+1)} = \mathbf{q}'^{(k)} - \left(\frac{\partial \boldsymbol{\delta}}{\partial \mathbf{q}}(\mathbf{q}'^{(k)}) \right)^+ \boldsymbol{\delta}(\mathbf{q}'^{(k)}) \quad (20)$$

The same least-squares procedure is also performed to project the initial condition onto the nonlinear approximation manifold. Importantly, the formulation of both LSPG projection and ECSW hyperreduction remains unchanged for any choice of nonlinear map \mathcal{N} .

3. Machine learning regression methods

3.1. Artificial neural network regression

So far, the map defined in (6) has been constructed using a deep ANN, as detailed in [18, 4] and summarized below.

From the solution approximation (7) and the orthogonality conditions (3), the vectors of primary and secondary generalized coordinates associated with the pre-computed solution snapshots can be computed

through projection as follows

$$\mathbf{q}^s = \mathbf{V}^T (\mathbf{u}^s - \mathbf{u}_{\text{ref}}), \quad \bar{\mathbf{q}}^s = \bar{\mathbf{V}}^T (\mathbf{u}^s - \mathbf{u}_{\text{ref}}), \quad s = 1, \dots, N_s \quad (21)$$

Substituting these generalized coordinates back into (7) and requiring exact reproduction of the solution snapshots leads to

$$\mathbf{u}^s - \mathbf{u}_{\text{ref}} = \mathbf{V}\mathbf{q}^s + \bar{\mathbf{V}}\mathcal{N}(\mathbf{q}^s), \quad s = 1, \dots, N_s \quad (22)$$

Pre-multiplying (22) by $\bar{\mathbf{V}}^T$ and utilizing the orthogonality conditions (3) results in

$$\bar{\mathbf{V}}^T (\mathbf{u}^s - \mathbf{u}_{\text{ref}}) = \mathcal{N}(\mathbf{q}^s)$$

which, in view of the projection definitions in (21), gives the relationship between the secondary and primary coordinates

$$\bar{\mathbf{q}}^s = \mathcal{N}(\mathbf{q}^s), \quad s = 1, \dots, N_s$$

Consequently, the ANN representing the map (6) is trained using the dataset of primary generalized coordinates $\{\mathbf{q}^s\}_{s=1}^{N_s}$ (or a subset thereof) as input to predict the corresponding secondary generalized coordinates $\{\bar{\mathbf{q}}^s\}_{s=1}^{N_s}$ (or a subset thereof). The ANN's vector-valued parameter $\boldsymbol{\eta}$ is determined by minimizing the following loss function over the training data

$$\boldsymbol{\eta} = \arg \min_{\boldsymbol{\eta}'} \frac{1}{N'_s} \sum_{s=1}^{N'_s} \|\bar{\mathbf{q}}^s - \mathcal{N}(\mathbf{q}^s, \boldsymbol{\eta}')\|_2^2$$

where N'_s represents the number of solution snapshots used for training. While N'_s is typically equal to the total number of snapshots N_s , it can be less ($N'_s < N_s$) when a very large dataset is collected, for example, from unsteady computations. In such cases, the specific subset of snapshots chosen for training does not imply any particular ordering from the original dataset.

This work investigates the suitability of deep ANNs (as in [18] or, more generally, ANNs of any architecture) as the primary regression method for constructing the map (6). This inquiry is motivated by two key limitations of deep ANNs within PMOR via latent space closure error modeling: their inherent opacity, complicating the development of rigorous theoretical a priori error estimates or indicators for the solution approximation (7), and the challenge of limited training data when seeking high accuracy with a very small number of high-dimensional solution snapshots N_s , resulting in an extremely small dimension n of the primary ROB \mathbf{V} – a scenario highly desirable for efficiency.

As an illustrative example, consider the benchmark steady hypersonic flow problem from [4], parameterized by a single free-stream Mach number ($N_{\mathcal{D}} = 1$). Traditional PMOR based on an affine approximation required a mere $N_s = 17$ steady solution snapshots to construct an accurate PROM of dimension $n_{\text{tra}} = 16$ across the entire considered parameter domain \mathcal{D} . Furthermore, the PMOR framework employing a deep ANN for the map (6) demonstrated the capability to reduce the HDM dimension from $N = 654\,720$ to $n = 2$ (with $\bar{n} = 14$) while maintaining comparable accuracy within \mathcal{D} . However, training this deep ANN necessitated the reconstruction of additional high-dimensional steady solution snapshots. A practical strategy to mitigate this involves leveraging the pre-computed total ROB $\mathbf{V}_{\text{tot}} = [\mathbf{V} \ \bar{\mathbf{V}}]$ (for this example, of dimension $n_{\text{tra}} = 16$) and the ECSW-generated reduced mesh based on \mathbf{V}_{tot} to build a traditional HPROM for the rapid reconstruction of these additional high-dimensional snapshots. This sufficiently fast offline strategy was successfully employed to construct an accurate HPROM-ANN of dimension $n = 2$ for the aforementioned hypersonic flow problem.

Nevertheless, the requirement to generate or reconstruct additional high-dimensional solution snapshots to facilitate the learning of the closure error using a deep ANN, while perhaps a minor inconvenience, remains a desirable aspect to eliminate.

To explore the potential of simpler regression methods as an alternative to deep ANNs in this context, the solution of the two-dimensional parametric inviscid Burgers problem, as presented in [18] and further detailed in Section 4 of this paper, is considered. This problem, defined over a two-dimensional parameter domain ($N_{\mathcal{D}} = 2$), features shocks propagating across the entire computational domain in both directions.

The construction of the map (6) is investigated using both a deep ANN and, for comparison, a single-layer ANN. The underlying hypothesis is that if an HPROM-ANN configured with a single-layer ANN can yield comparable levels of accuracy and efficiency to its counterpart configured with a deep ANN for a given small dimension n of the primary ROB \mathbf{V} , it would suggest that a simpler regression method, such as GPR, could also achieve similar accuracy in this context.

Specifically, the instance of this problem considered herein involves a high-dimensional model (based on a finite volume discretization) with a dimension of $N = 125\,000$. The HPROM-ANN is configured with a primary ROB dimension of $n = 10$ and a secondary ROB dimension of $\bar{n} = 140$. For the single-layer ANN, the architecture comprises one hidden layer with 1 400 neurons and ELU activation. In contrast, the multi-layer ANN replicates the architecture described in [18], consisting of six ELU-activated layers with sizes (10, 32, 64, 128, 256, 256, 140). Both networks are trained using the same dataset of 4 501 snapshot pairs $(\mathbf{q}, \bar{\mathbf{q}})$, generated by sampling the two-dimensional parameter domain $\mathcal{D} = [4.25, 5.50] \times [0.015, 0.03]$ at 9 distinct points, and for each of these parameter points, sampling the temporal solution in the time interval $[0, 25]$ at 500 equidistant points. In both cases, 90% of the dataset is allocated for training and 10% for validation.

Table 1 summarizes the performance of the two HPROM-ANN configurations detailed above. Figure 1 presents a qualitative comparison between the solutions predicted by the HDM and both HPROM-ANN configurations at a specific time $t \in]0, 25[$ and along two different slices of the computational domain. The results reported in this table and figure demonstrate that, within the context of an affine approximation with latent space closure error modeling, a shallow ANN and a deep ANN yield comparable efficiency and accuracy for the HPROM-ANN. These findings, along with numerous similar observations by the authors regarding the performance of HPROM-ANNs configured with single-layer and multi-layer ANNs for constructing the map (6), and the inherent opacity of ANNs that hinders the development of rigorous theoretical a priori error estimates or indicators for their use in PMOR, constitute the primary motivation for the alternative machine learning regression models developed in the subsequent two sections of this paper.

Parameter (μ_1, μ_2)	Relative global Euclidean error (%)		Wall-clock time (minutes)	
	HPROM-ANN (single-layer)	HPROM-ANN (multi-layer)	HPROM-ANN (single-layer)	HPROM-ANN (multi-layer)
(4.56, 0.019)	1.81	1.07	0.29	0.28
(4.75, 0.020)	1.22	0.68	0.30	0.29
(5.19, 0.026)	2.29	1.83	0.32	0.30

Table 1: Online performance comparison (accuracy and computational speedups) of two different HPROM-ANN configurations for the 2D parametric inviscid Burgers’ problem at three out-of-sample parameter points ($n = 10$, $\bar{n} = 140$, single core).

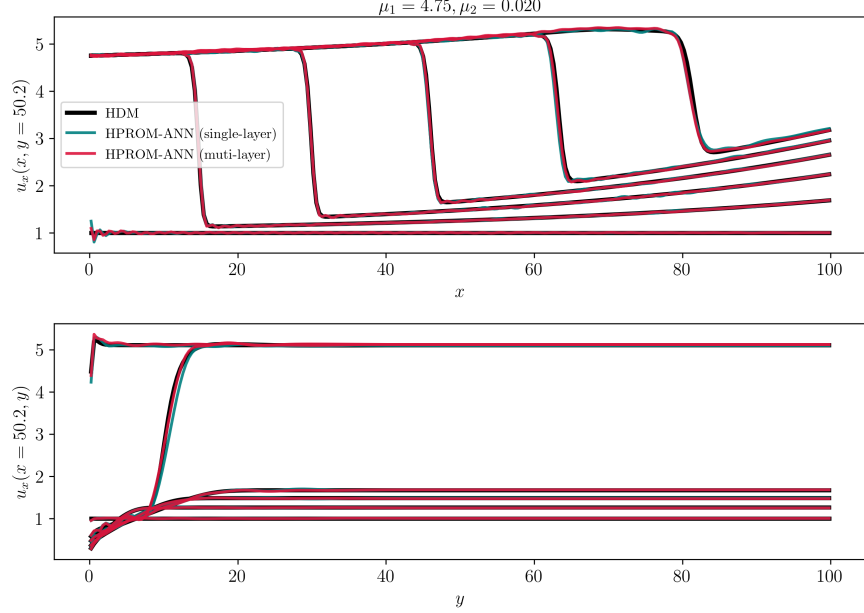


Figure 1: Solution slices predicted for out-of-sample parameter point $\boldsymbol{\mu} = (4.75, 0.020)$ at the time steps $t = 0, 5, 10, 15, 20,$ and 25 using HDM, HPRM-ANN configured with a single-layer ANN, and HPRM-ANN configured with a multi-layer ANN: $y = 50.2$ (top); $x = 50.2$ (bottom).

3.2. Gaussian process regression

GPR is first considered as an interpretable and robust alternative to (deep) ANN models for constructing the nonlinear map \mathcal{N} from primary to secondary generalized coordinates, particularly in data-scarce contexts.

Mean regressor. Gaussian processes (GPs) have recently gained popularity in machine learning for classification tasks, and have long served as a regression tool, widely known as kriging [24]. A GP is a collection of normal random variables $Y(\mathbf{x})$, indexed by a d -dimensional vector \mathbf{x} , such that any finite subset of these variables has a multivariate normal distribution. A GP is fully characterized by its mean function, $m(\mathbf{x}) = \mathbb{E}[Y(\mathbf{x})]$, where \mathbb{E} denotes mathematical expectation, and its covariance function

$$K(\mathbf{x}, \mathbf{x}') = \text{cov}(Y(\mathbf{x}), Y(\mathbf{x}')) = \mathbb{E}[(Y(\mathbf{x}) - m(\mathbf{x}))(Y(\mathbf{x}') - m(\mathbf{x}'))] \quad (23)$$

This covariance function is often simply called the kernel. For regression, training data acts as a prior. Bayesian posterior predictions, given this training data, also form a GP whose mean and covariance functions are easily computed [25]. For simplicity, assuming a zero-mean GP $\xi \sim \mathcal{N}(0, K)$ with covariance kernel K , an unknown response function $f^\dagger: \mathbb{R}^d \rightarrow \mathbb{R}$ can be approximated from measurements $f^\dagger(\mathbf{x}^s) = y^s$, for $s = 1, \dots, N_{\text{td}}$, where N_{td} denotes the number of training data points. This approximation is given by the regressor

$$f(\mathbf{x}) = \mathbb{E}[\xi(\mathbf{x}) | \xi(\mathbf{x}^s) = y^s, s = 1, \dots, N_{\text{td}}] = \mathbf{K}(\mathbf{x}, \mathbf{X})\mathbf{K}^{-1}(\mathbf{X}, \mathbf{X})\mathbf{y} \quad (24)$$

where $\mathbf{K}(\mathbf{X}, \mathbf{X})$ is the $N_{\text{td}} \times N_{\text{td}}$ matrix with entries $K(\mathbf{x}^s, \mathbf{x}^r)$, and $\mathbf{K}(\mathbf{x}, \mathbf{X})$ is the N_{td} -dimensional row vector with entries $K(\mathbf{x}, \mathbf{x}^s)$, for $s, r = 1, \dots, N_{\text{td}}$.

The regressor (24) represents the mean of the conditional GP, with its variance given by

$$\sigma^2(\mathbf{x}) = \text{Var}(\xi(\mathbf{x}) | \xi(\mathbf{x}^s) = y^s, s = 1, \dots, N_{\text{td}}) = K(\mathbf{x}, \mathbf{x}) - \mathbf{K}(\mathbf{x}, \mathbf{X})\mathbf{K}^{-1}(\mathbf{X}, \mathbf{X})\mathbf{K}^T(\mathbf{x}, \mathbf{X}) \quad (25)$$

The choice of kernel can be tailored to a particular dataset to capture varying degrees of smoothness or other known prior properties of the data. While the squared exponential (Gaussian) kernel is arguably the most popular, other common choices include inverse quadratic, rational quadratic, constant (white noise), and the Matérn family of kernels. For instance, the Matérn kernel with a smoothness parameter $\nu = 1.5$

precisely matches the kernel

$$K(\mathbf{x}, \mathbf{x}') = \sigma_f^2 \left(1 + \frac{\sqrt{3}\|\mathbf{x} - \mathbf{x}'\|_2}{\ell} \right) \exp \left(-\frac{\sqrt{3}\|\mathbf{x} - \mathbf{x}'\|_2}{\ell} \right)$$

which is employed in the numerical assessments performed in Section 4. Here, σ_f^2 serves as a hyperparameter for the signal variance, and ℓ is another hyperparameter defining an isotropic length-scale of correlation in the input space. Anisotropic kernels are often considered to account for differing behavior across input space dimensions, assigning a separate length-scale for each. Kernels can also be combined multiplicatively and additively to form composite kernels, further enhancing the prior of the approximation.

The resulting GP model is often described as nonparametric because, apart from the chosen kernel and its hyperparameters, it depends solely on the training data. Cross-validation or maximizing the marginal log-likelihood [25] are the most popular techniques for estimating hyperparameter values. The latter method yields an explicit analytic formula amenable to gradient-based optimization. Its effect can be likened to favoring the least complex model that explains the data.

While vector GPs have been investigated, cross-output correlations are frequently disregarded for simplicity, leading to each output dimension being represented by a standard, scalar-valued GP. To further reduce computational workload in this work, it is also assumed that these scalar-valued GPs share a common kernel defined by the same hyperparameters.

The GPR model is trained using the data described in Section 3.1, where each high-dimensional solution snapshot \mathbf{u}^s is mapped to its corresponding pair of primary and secondary generalized coordinates $(\mathbf{q}^s, \bar{\mathbf{q}}^s)$. These pairs are then assembled into the training matrices

$$\mathbf{Q}_{\text{td}} = \begin{bmatrix} (\mathbf{q}^1)^T \\ (\mathbf{q}^2)^T \\ \vdots \\ (\mathbf{q}^{N_{\text{td}}})^T \end{bmatrix} \in \mathbb{R}^{N_{\text{td}} \times n}, \quad \bar{\mathbf{Q}}_{\text{td}} = \begin{bmatrix} (\bar{\mathbf{q}}^1)^T \\ (\bar{\mathbf{q}}^2)^T \\ \vdots \\ (\bar{\mathbf{q}}^{N_{\text{td}}})^T \end{bmatrix} \in \mathbb{R}^{N_{\text{td}} \times \bar{n}}$$

Here, $N_{\text{td}} = N'_s$, which denotes the chosen number of training snapshots and satisfies $N'_s \leq N_s$ (see Section 3.1). In the predictive (online) phase, the value of the nonlinear closure map $\mathcal{N}(\mathbf{q}^*) \in \mathbb{R}^{\bar{n}}$ at a new primary coordinate $\mathbf{q}^* \in \mathbb{R}^n$ is obtained by vectorizing (24) and applying the single-kernel assumption as

$$\mathcal{N}(\mathbf{q}^*)^T = \mathbf{K}(\mathbf{q}^*, \mathbf{Q}_{\text{td}}) (\mathbf{K}(\mathbf{Q}_{\text{td}}, \mathbf{Q}_{\text{td}}) + \sigma_{ng}^2 \mathbf{I})^{-1} \bar{\mathbf{Q}}_{\text{td}} \quad (26)$$

Here, σ_{ng}^2 represents the Gaussian noise variance, often called a ‘‘nugget.’’ This term is crucial for two reasons: it helps limit overfitting and enhances numerical stability. $\mathbf{I} \in \mathbb{R}^{N'_s \times N'_s}$ is the identity matrix.

This formulation naturally supports an offline-online decomposition. First, the matrix $\boldsymbol{\alpha} \in \mathbb{R}^{N'_s \times \bar{n}}$ is computed offline as follows

$$\boldsymbol{\alpha} = (\mathbf{K}(\mathbf{Q}_{\text{td}}, \mathbf{Q}_{\text{td}}) + \sigma_{ng}^2 \mathbf{I})^{-1} \bar{\mathbf{Q}}_{\text{td}} \quad (27)$$

Each online prediction then requires only the evaluation of $\mathbf{K}(\mathbf{q}^*, \mathbf{Q}_{\text{td}})$ and a matrix-vector multiplication.

Beyond the mean prediction, the GP model provides a prediction of uncertainty in the form of an input space parameter-dependent variance, which can be obtained from (25). While not exploited in the present work, this variance is often used as an error indicator and to guide adaptive sampling [26].

Analytical Jacobians for GPR. As a PMOR method for implicit discrete systems, LSPG [8, 9] necessitates the evaluation of the Jacobian of the approximation given in (7) with respect to \mathbf{q} . This, in turn, requires computing the Jacobian of the nonlinear map \mathcal{N} with respect to \mathbf{q} . Fortunately, a closed-form expression for this Jacobian can be derived.

Specifically, utilizing the precomputed weight matrix $\boldsymbol{\alpha}$ from (27), the Jacobian of \mathcal{N} with respect to \mathbf{q}^* is

$$\frac{\partial \mathcal{N}}{\partial \mathbf{q}^*} = \boldsymbol{\alpha}^T \mathbf{J}_K(\mathbf{q}^*) \quad (28)$$

where $\partial\mathcal{N}/\partial\mathbf{q}^* \in \mathbb{R}^{\bar{n} \times n}$, and $\mathbf{J}_K(\mathbf{q}^*) \in \mathbb{R}^{N'_s \times n}$ is defined entry-wise as

$$[\mathbf{J}_K(\mathbf{q}^*)]_{si} = \frac{\partial K(\mathbf{q}^*, \mathbf{q}^s)}{\partial q_i^*} \quad (29)$$

For the Matérn kernel with $\nu = 1.5$, $[\mathbf{J}_K(\mathbf{q}^*)]_{si}$ can be evaluated analytically as

$$[\mathbf{J}_K(\mathbf{q}^*)]_{si} = -3 \frac{\sigma_f^2}{\ell^2} \exp(-\sqrt{3}d_s) (q_i^* - q_i^s), \quad d_s = \frac{\|\mathbf{q}^* - \mathbf{q}^s\|_2}{\ell}$$

In cases where a selected kernel cannot be differentiated analytically, its Jacobian can be computed using numerical differentiation.

To summarize, GPR offers several key advantages, including gradient-based hyperparameter optimization, the availability of analytical derivatives, and a principled approach to estimating epistemic uncertainty. In the current work, a single multi-output formulation is employed. This approach avoids the computational burden associated with fitting \bar{n} separate scalar GPs. As the online prediction stage relies solely on the posterior mean, the resulting closure operates deterministically.

3.3. Radial basis function interpolation

Next, RBF interpolation is considered as another interpretable and robust alternative to (deep) ANNs for latent space closure error modeling, particularly in data-scarce scenarios. This approach offers a fully deterministic regression model [27] that maintains the closed-form structure and analytical derivatives characteristic of GPR. However, it forgoes all probabilistic components, including marginal-likelihood-based hyperparameter training and predictive variance modeling.

RBF interpolant. RBF interpolation inherently handles vector-valued outputs, providing a scalable solution when uncertainty quantification is not a priority. It approximates a function by using a weighted linear combination of radial kernel functions centered at the training input points

$$\sum_{s=1}^{N_{\text{td}}} \mathbf{w}^s \phi(\|\mathbf{x} - \mathbf{x}^s\|_2)$$

where $\phi : [0, \infty) \rightarrow \mathbb{R}$ is a RBF. Common RBF kernels include the Gaussian ($\phi(r) = \exp(-\epsilon^2 r^2)$), multi-quadratic ($\phi(r) = \sqrt{1 + (\epsilon r)^2}$), and inverse multiquadratic ($\phi(r) = (1 + (\epsilon r)^2)^{-1/2}$) kernels, where ϵ is a shape parameter.

An RBF interpolant coincides with the regressor derived from GPR when using a stationary kernel, i.e., one satisfying $K(\mathbf{x}, \mathbf{x}') = \phi(\|\mathbf{x} - \mathbf{x}'\|)$, as seen in (23). Consequently, approximating the nonlinear closure map $\mathcal{N} : \mathbb{R}^n \rightarrow \mathbb{R}^{\bar{n}}$ using RBF interpolation formally leads to an expression mirroring (26)

$$\mathcal{N}(\mathbf{q}^*)^T = \mathbf{K}(\mathbf{q}^*, \mathbf{Q}_{\text{td}}) (\mathbf{K}(\mathbf{Q}_{\text{td}}, \mathbf{Q}_{\text{td}}) + \lambda \mathbf{I})^{-1} \bar{\mathbf{Q}}_{\text{td}}$$

In this context, $\mathbf{K}(\mathbf{q}^*, \mathbf{Q}_{\text{td}}) \in \mathbb{R}^{1 \times N'_s}$ is a row vector containing RBF kernel evaluations with entries $[\mathbf{K}(\mathbf{q}^*, \mathbf{Q}_{\text{td}})]_s = \phi(\|\mathbf{q}^* - \mathbf{q}^s\|_2)$. The symmetric matrix $\mathbf{K}(\mathbf{Q}_{\text{td}}, \mathbf{Q}_{\text{td}}) \in \mathbb{R}^{N'_s \times N'_s}$ is defined by $[\mathbf{K}(\mathbf{Q}_{\text{td}}, \mathbf{Q}_{\text{td}})]_{sr} = \phi(\|\mathbf{q}^s - \mathbf{q}^r\|_2)$. The term $\lambda \mathbf{I}$ acts as a regularization term, introduced solely for numerical stability.

As with GPR, this formulation supports an efficient offline-online framework. The interpolation weights $\boldsymbol{\beta} \in \mathbb{R}^{N'_s \times \bar{n}}$ are precomputed offline by solving a system with multiple right-hand sides

$$(\mathbf{K}(\mathbf{Q}_{\text{td}}, \mathbf{Q}_{\text{td}}) + \lambda \mathbf{I}) \boldsymbol{\beta} = \bar{\mathbf{Q}}_{\text{td}}$$

Online predictions then only require N'_s kernel evaluations and a matrix-vector product, $\mathcal{N}(\mathbf{q}^*) = \mathbf{K}(\mathbf{q}^*, \mathbf{Q}_{\text{td}}) \boldsymbol{\beta}$.

It is important to note that the regularization parameter λ , unlike the noise variance σ_{ng}^2 in GPR, is not derived from a probabilistic model; its role is purely for numerical stabilization. The kernel hyperparameter ϵ is selected by cross-validation in conjunction with a search procedure rather than via marginal likelihood maximization.

Analytical Jacobians for RBF interpolation. Like GPR (see (28)–(29)), the deterministic RBF interpolant

also admits analytical Jacobians. The Jacobian of the nonlinear map \mathcal{N} is given by

$$\frac{\partial \mathcal{N}}{\partial \mathbf{q}}(\mathbf{q}^*) = \beta^T \mathbf{J}_\phi(\mathbf{q}^*)$$

where the Jacobian matrix $\mathbf{J}_\phi(\mathbf{q}^*) \in \mathbb{R}^{N'_s \times n}$ has entries

$$[\mathbf{J}_\phi(\mathbf{q}^*)]_{si} = \frac{\partial \phi(\|\mathbf{q}^* - \mathbf{q}^s\|_2)}{\partial q_i^s} = \phi'(\|\mathbf{q}^* - \mathbf{q}^s\|_2) \frac{q_i^* - q_i^s}{\|\mathbf{q}^* - \mathbf{q}^s\|_2}$$

and $\phi'(\cdot)$ denotes the radial derivative of the RBF kernel. For instance, with the Gaussian kernel, this derivative is

$$\phi'(r) = -2\epsilon^2 r \exp(-\epsilon^2 r^2)$$

4. Applications and performance assessments

All nonlinear model reduction methods discussed in this paper were implemented in the finite volume (FV) compressible flow solver AERO-F [28] and integrated into its existing PMOR capabilities. This solver includes a low-Mach preconditioner [29] specifically designed for low-speed flows. The PROMs are constructed using the LSPG projection method and hyperreduced with ECSW. The effectiveness of these model reduction and hyperreduction methods is evaluated using two representative CFD applications.

The first application can be easily reproduced by interested readers, as it involves solving an inviscid Burgers problem formulated in a two-dimensional (2D) square and parameterized over a 2D parameter domain \mathcal{D} ($N_{\mathcal{D}} = 2$). It is programmed in Python. It features shocks that propagate across the entire domain in both directions, making it particularly challenging not only for traditional PMOR approaches based on the affine approximation of the solution but also for many otherwise promising nonlinear PMOR techniques, such as registration methods based on shock-fitting.

The second application serves as a benchmark problem for CFD in the automotive industry, making it highly representative of industrial challenges. It focuses on simulating the turbulent flow over a specific configuration of the Ahmed body using the DES turbulence model. In this case, time is the only considered parameter and thus $N_{\mathcal{D}} = 1$, and all numerical simulations are performed using AERO-F.

For time-dependent simulations and in the presence of strong shocks, some studies [4] advocate for alternative accuracy assessment approaches beyond the global infinity norm, L^2 norm, or Euclidean norm. Examples include adaptations of the quadratic Wasserstein distance [30] to deterministic settings [31], or the dynamic time-warping distance measure [32]. However, given that the propagating shocks in the first application are relatively weak compared to those in [4], which focuses on hypersonic flows, and are nearly absent in the second application, this study adopts primarily the simpler and more interpretable global Euclidean norm for accuracy assessment. Specifically, the relative error associated with an approximate solution predicted using a reduced-order model is computed as

$$\mathbb{RE}_{2, \text{QoI}}(\boldsymbol{\mu}^*) = \frac{\sqrt{\sum_{m=0}^{N_t} \left\| \text{QoI}^m(\boldsymbol{\mu}^*) - \widetilde{\text{QoI}}^m(\boldsymbol{\mu}^*) \right\|_2^2}}{\sqrt{\sum_{m=0}^{N_t} \left\| \text{QoI}^m(\boldsymbol{\mu}^*) \right\|_2^2}} \quad (30)$$

where:

- QoI^m denotes a scalar or vector quantity of interest computed at time step t^m by post-processing the high-dimensional solution \mathbf{u}^m . This could include the solution vector \mathbf{u}^m itself.
- $\widetilde{\text{QoI}}^m$ represents the counterpart of QoI^m computed using the approximate solution $\tilde{\mathbf{u}}^m$ obtained from a reduced-order or hyper-reduced-order model.
- $\boldsymbol{\mu}^*$ and N_t denote, as before, a queried but unsampled parameter point in \mathcal{D} and the total number of computational time steps (excluding the initial time step), respectively.

All computations reported in this section were performed in double-precision arithmetic on a Linux cluster, where each node is equipped with two Intel Xeon Gold 5118 processors (24 physical cores in total) clocked at 2.3 GHz and 192 GB of memory. Unless otherwise specified, all offline (training) costs – except for the generation of high-dimensional solution snapshots – and all online (solution) costs are reported as wall-clock timings measured on a single node of the aforementioned cluster.

4.1. Two-dimensional parametric inviscid Burgers problem

4.1.1. Problem setup and discretization

The 2D parametric inviscid Burgers initial-boundary-value problem (IBVP) and parameter settings originally introduced in [18] are adopted in this study. The same 2D configuration is precisely reproduced to enable direct comparisons and verifications against the results obtained using the PROM-ANN model presented in the referenced work. Specifically, the following IBVP is considered

$$\begin{aligned}
 \frac{\partial u_x}{\partial t} + u_x \frac{\partial u_x}{\partial x} + u_y \frac{\partial u_x}{\partial y} &= 0.02 \exp(\mu_2, x) \\
 \frac{\partial u_y}{\partial t} + u_x \frac{\partial u_y}{\partial x} + u_y \frac{\partial u_y}{\partial y} &= 0 \\
 u_x(0, y, t; \boldsymbol{\mu}) &= \mu_1 \\
 u_x(x, y, 0) = 1, \quad u_y(x, y, 0) &= 1 \\
 t &\in (0, T_f]
 \end{aligned} \tag{31}$$

where $\boldsymbol{\mu} = (\mu_1, \mu_2)$ is the parameter vector. The parameter μ_1 influences the left boundary condition $u_x(0, y, t; \boldsymbol{\mu})$, while μ_2 appears in the source term of the first equation in (31). Both parameters directly impact the formation and propagation of shock waves within the computational domain Ω .

The spatial domain is given by $\Omega = [0, 100] \times [0, 100]$, while the parameter domain is chosen as $\mathcal{D} = [4.25, 5.50] \times [0.015, 0.03]$. This selection ensures that the solution $u = [u_x \ u_y]^T$ of (31) exhibits shock waves propagating throughout Ω , both from left to right and from top to bottom. The presence of these traveling discontinuities significantly limits the low-rank approximability of the solution set, as dictated by the Kolmogorov n -width barrier. As a result, efficiently solving this problem typically requires a nonlinear model-reduction approach capable of handling long-range shock wave propagation. The temporal domain is set to $(0, T_f] = (0, 25]$.

For spatial discretization, the square domain Ω is partitioned into a uniform, structured mesh consisting of 250×250 equally sized elements (primal cells), yielding a total of $N_e = 62\,500$ elements and a state-space dimension of $N = 125\,000$. The IBVP (31) is semi-discretized using a cell-centered FV Godunov method, producing the semi-discrete solution vector $\mathbf{u} \in \mathbb{R}^N$.

The time interval $(0, T_f]$ is divided into 500 equally spaced steps of size $\Delta t = 0.05$. The semi-discrete form of (31) is then integrated in time using the midpoint rule. Within each time step, the resulting system of nonlinear algebraic equations is solved using a direct sparse solver.

On a Linux cluster with the previously described hardware configuration, each HDM simulation requires approximately 12.79 minutes of wall-clock time to complete.

4.1.2. Construction, training, and partitioning of the reduced-order basis and nonlinear maps

Solution snapshots from HDM are first collected. Following the work in [18], the parameter domain \mathcal{D} is uniformly sampled on a 3×3 grid through constant increments $\Delta\mu_1 = 0.625$ and $\Delta\mu_2 = 0.0075$. For each of the nine sampled parameter points, the corresponding HDM is run over the time interval $t \in (0, 25]$, with a fixed time step $\Delta t = 0.05$ (for a total of 500 time steps). This procedure produces $N_s = 4\,501$ solution snapshots in total, including the shared initial condition.

The solution snapshots are stored in the matrix $\mathbf{S} \in \mathbb{R}^{N \times 4\,501}$, and a thin SVD is computed. Following the standard energy-based truncation criterion with $\varepsilon_S^2 = 5\%$, $n_{\text{tra}} = 95$ modes are first retained to form the traditional ROB $\mathbf{V} \in \mathbb{R}^{N \times 95}$. To construct nonlinear PROMs, $n = 10$ retained modes of this basis are retained and complemented by $\bar{n} = 140$ discarded modes, resulting in a pair of ROBs $\mathbf{V} \in \mathbb{R}^{N \times 10}$ and $\bar{\mathbf{V}} \in \mathbb{R}^{N \times 140}$ that delivers an accuracy comparable to that of the $n_{\text{tra}} = 95$ PROM, consistent with [18].

4.1.3. Common training data and latent-space pairs

To train each nonlinear PROM, the procedure outlined in Section 2 is followed to map each high-dimensional solution snapshot to a pair of latent-coordinate vectors $(\mathbf{q}, \bar{\mathbf{q}})$. These latent pairs collectively form a shared dataset of training inputs $\mathbf{Q}_{\text{td}} \in \mathbb{R}^{4501 \times 10}$ and corresponding outputs $\bar{\mathbf{Q}}_{\text{td}} \in \mathbb{R}^{4501 \times 140}$.

The neural-network closure approach from [18] is replicated here, where \mathcal{N} is implemented using a feedforward fully connected multi-layer perceptron (MLP) architecture. In this case, the input and output sizes are $n = 10$ and $\bar{n} = 140$, respectively, and the network consists of six linear layers with exponential linear unit (ELU) activations. Specifically, the sizes of these layers are

$$(n, 32) \xrightarrow{\text{ELU}} (32, 64) \xrightarrow{\text{ELU}} (64, 128) \xrightarrow{\text{ELU}} (128, 256) \xrightarrow{\text{ELU}} (256, 256) \xrightarrow{\text{ELU}} (256, \bar{n}) \quad (32)$$

All $(\mathbf{q}, \bar{\mathbf{q}})$ pairs from the entire snapshot set (totaling 4501 in this case) are gathered and randomly shuffled, and then 90% of them are allocated for training the surrogate while 10% are used for validation. The MLP is implemented in PyTorch and trained using a mean-squared error (MSE) loss: training was completed in approximately 19.3 minutes on 24 cores of the same node of the Linux cluster. The Gaussian-process nonlinear closure is constructed by training a single multi-output GPR model on the previously described latent-space dataset. A composite kernel is adopted, consisting of a Matérn kernel with smoothness parameter $\nu = 1.5$, scaled by a constant kernel (signal variance σ_f^2), and augmented with a white-noise kernel (noise variance σ_{ng}^2). The signal variance σ_f^2 is optimized within the bounds $(10^{-3}, 10^2)$, the Matérn length-scale ℓ is initialized to 0.5 with bounds $(10^{-2}, 5.0)$, and the noise variance is fixed at $\sigma_{ng}^2 = 10^{-5}$. The primary generalized coordinates are normalized using Min-Max scaling within the range $(-1, 1)$, while the secondary generalized coordinates remain unscaled. GPR training is performed using the limited-memory Broyden-Fletcher-Goldfarb-Shanno (L-BFGS-B) optimizer from the `scikit-learn` library, taking approximately 96.08 minutes on 24 cores of the same node of the Linux cluster. The optimized hyperparameters obtained after training include a constant kernel value of 10^2 and a Matérn kernel length-scale of $\ell = 0.814$.

A nonlinear closure based on RBF interpolation is likewise established by training a multi-output RBF regression model using the common latent-space dataset. Specifically, Gaussian, inverse multiquadric, multiquadric, and linear RBF kernels are considered. An iterative search procedure is employed to select the optimal kernel type, the shape parameter (ϵ) within bounds $(0.2, 5)$, and the regularization parameter (λ) within bounds $(10^{-12}, 10^{-6})$, by minimizing a cross-validation error measure. The scaling strategy for the primary and secondary generalized coordinates follows the same approach as that used for the GPR closure. This iterative search is implemented with four-fold cross-validation using the Expected Improvement acquisition function provided by the `scikit-optimize` library. Training and optimization on a 24-core CPU node of the Linux cluster take approximately 13.24 minutes. The optimized hyperparameters obtained after training include the inverse multiquadric kernel, a shape parameter of $\epsilon = 2.42$, and a regularization parameter of $\lambda = 10^{-12}$.

4.1.4. Hyperreduction using the ECSW method

ECSW, which is particularly effective for unsteady applications [6], is used to hyperreduce each considered reduced-order model by training this hyperreduction method on the projected residuals. Specifically, the ECSW training is conducted using a single parameter combination of $(4.25, 0.0225)$ and takes every 10th snapshot from the collected solution trajectories. The ECSW procedure is executed separately for the traditional PROM and each nonlinear PROM, which incorporates ANN, GPR, or RBF for closure modeling, with the training tolerance consistently set to $\varepsilon_{\text{ECSW}} = 10^{-14}$. For the traditional PROM, ECSW results in a considerably larger reduced mesh comprised of $n_e = 5746$ elements. In contrast, ECSW generates distinctly smaller reduced meshes for each nonlinear PROM: 1496 elements for HPROM-ANN, 1483 elements for HPROM-GPR, and 1487 elements for HPROM-RBF (see Table 2). The advantageous behavior of ECSW, as observed with PROM-ANNs and generally applicable to all nonlinear PROMs discussed in this paper, is rigorously explained in [16, 18].

4.1.5. Performance comparisons

The accuracy and computational efficiency of the four model reduction methods under consideration are evaluated at three unsampled parameter points: $\boldsymbol{\mu}_1 = (4.75, 0.02)$, $\boldsymbol{\mu}_2 = (4.56, 0.019)$, and $\boldsymbol{\mu}_3 =$

Computational model	n	\bar{n}	n_e	Wall-clock time (min)
HPROM (ECSW)	95	-	5 746	128.72
HPROM-ANN (ANN)	10	140	-	19.30
HPROM-ANN (ECSW)	10	140	1 496	8.10
HPROM-GPR (GPR)	10	140	-	96.08
HPROM-GPR (ECSW)	10	140	1 483	7.70
HPROM-RBF (RBF)	10	140	-	13.24
HPROM-RBF (ECSW)	10	140	1 487	8.74

Table 2: Offline computational timings and ECSW-generated reduced mesh sizes for the traditional and nonlinear PROMs applied to the 2D parametric inviscid Burgers’ problem: ECSW computations and training of the nonlinear closures (ANN, GPR, and RBF) are conducted on 24 CPU cores.

(5.19, 0.026). The assessment uses the maximum relative error metric, defined as

$$\mathbb{RE}_{2, \text{QoI}}^{\max} = \max_{\boldsymbol{\mu}_1, \boldsymbol{\mu}_2, \boldsymbol{\mu}_3} \mathbb{RE}_{2, \text{QoI}}(\boldsymbol{\mu})$$

where the formulation of $\mathbb{RE}_{2, \text{QoI}}$ is provided in (30), and the QoI is chosen as the solution vector \mathbf{u} . Additionally, wall-clock computational times and speedup factors relative to HDM are summarized in Table 3.

Computational model	n (N for HDM)	\bar{n}	n_e (N_e for HDM)	$\mathbb{RE}_{2, \mathbf{u}}^{\max}$ (%)	Wall-clock time (minutes)	Speedup factor
HDM	125 000	-	62 500	-	12.75	-
HPROM	95	-	5 746	1.47	1.62	7.87
HPROM-ANN	10	140	1 496	1.83	0.29	43.35
HPROM-GPR	10	140	1 483	1.71	0.29	43.67
HPROM-RBF	10	140	1 487	1.66	0.27	47.13

Table 3: Online performance comparison (accuracy and computational speedups) of traditional and nonlinear HPROMs for the 2D parametric inviscid Burgers’ problem.

Samples of the solution time histories calculated at the three unsampled parameter points are provided to illustrate qualitative differences in shock-capturing performance between the traditional HPROM and the nonlinear HPROMs considered in this work.

Figure 2 presents an accuracy comparison at $\boldsymbol{\mu}_1 = (4.75, 0.020)$ between the traditional HPROM and HPROM-RBF. Both methods effectively capture the moving shock; however, the traditional HPROM exhibits noticeable oscillatory behavior, which is primarily due to its limited representation capabilities resulting from the affine approximation and truncation at 95 retained modes. In contrast, HPROM-RBF, utilizing 10 retained and 140 discarded modes, significantly reduces these oscillations. Moreover, HPROM-RBF demonstrates a remarkable improvement in computational efficiency, achieving an average speedup factor of 47.13, compared to the traditional HPROM’s speedup of 7.87.

Figure 3 compares the accuracy of HPROM-ANN and HPROM-GPR models at the parameter point $\boldsymbol{\mu}_2 = (4.56, 0.019)$. Both reduced-order models effectively track the shock, with HPROM-GPR yielding slightly smoother solutions. Additionally, both models achieve similar computational speedups: 43.35 for HPROM-ANN; and 43.67 for HPROM-GPR, benefiting from the analytical Jacobian provided by the closed-form expression of the Matérn kernel and the optimized automatic differentiation routines implemented in PyTorch.

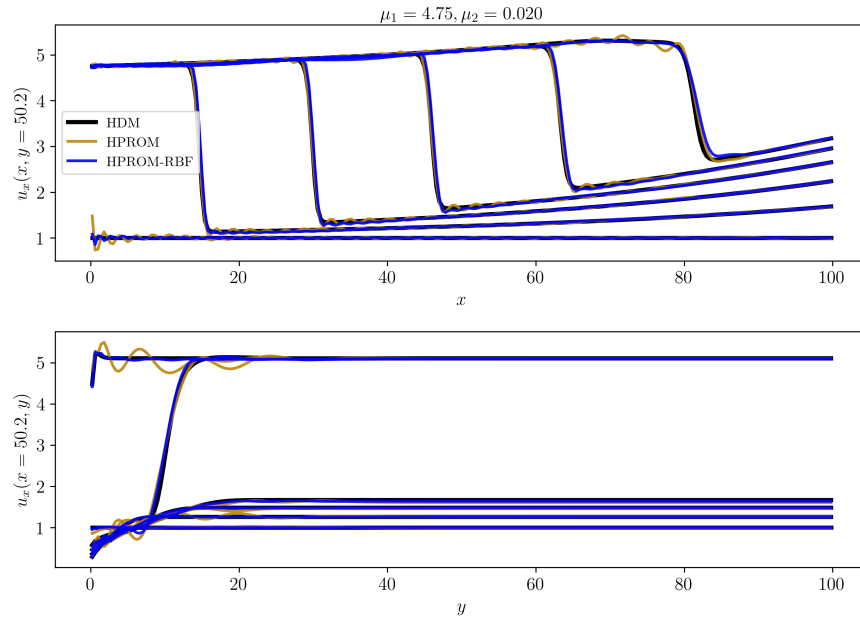


Figure 2: Solution slices predicted for $\mu_3 = (4.75, 0.020)$ at the time steps $t = 0, 5, 10, 15, 20,$ and 25 using HDM, HPROM, and HPROM-RBF: $y = 50.2$ (top); $x = 50.2$ (bottom).

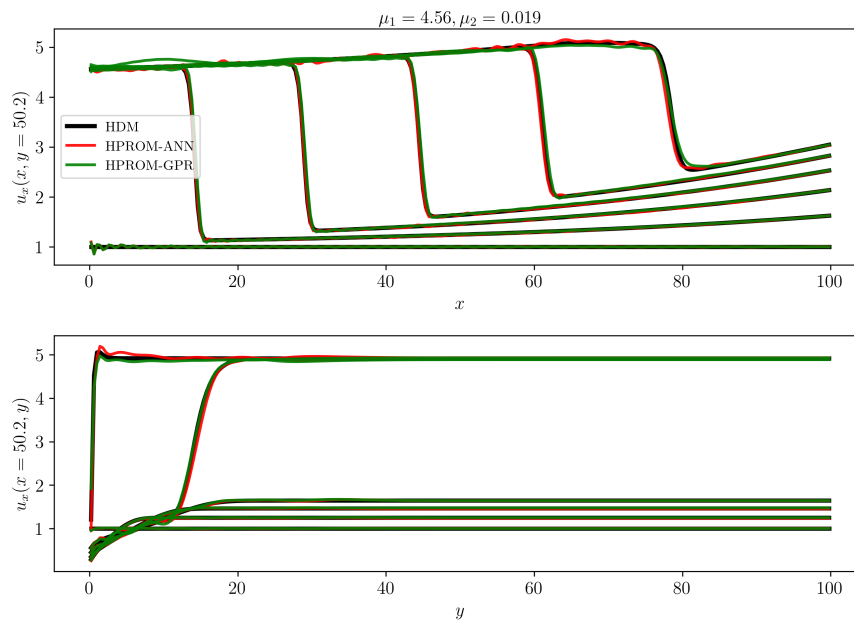


Figure 3: Solution slices predicted for $\mu_3 = (4.56, 0.019)$ at the time steps $t = 0, 5, 10, 15, 20,$ and 25 using HDM, HPROM-ANN, and HPROM-GPR: $y = 50.2$ (top); $x = 50.2$ (bottom).

Finally, Figure 4 provides an accuracy comparison of all three nonlinear reduced-order models at $\mu_3 = (5.19, 0.026)$, a test point that demonstrated the highest error. While all models effectively track the shock with comparable accuracy for most time steps, their performance noticeably deteriorates near the final time step. During this critical stage, each model encounters some difficulties in capturing the exact shock position; however, HPRM-ANN demonstrates a slightly better overall match with HDM, whereas the HPRM-GPR and HPRM-RBF solutions maintain smoothness and exhibit less oscillatory behavior. These observations suggest that both the HPRM-GPR and HPRM-RBF models serve as complementary alternatives to HPRM-ANN for modeling shock-dominated flow problems.

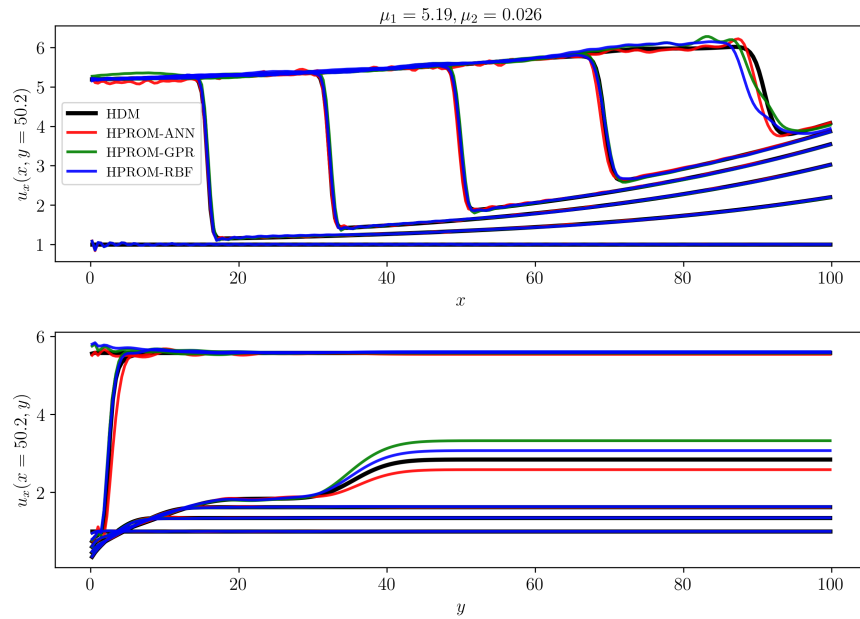


Figure 4: Solution slices predicted for $\mu_3 = (5.19, 0.026)$ at the time steps $t = 0, 5, 10, 15, 20,$ and 25 using HDM, HPRM-ANN, HPRM-GPR, and HPRM-RBF: $y = 50.2$ (top); $x = 50.2$ (bottom).

4.2. Ahmed body turbulent wake flow problem

The focus now shifts to a specific configuration of the Ahmed body and the rapid simulation of its turbulent wake using a DES turbulence model, with time as the sole parameter [33]. The unsteady nature of the wake flow, driven by turbulence, generates a sufficiently rich solution that enables observation of the Kolmogorov barrier and benchmarking of various reduced-order models. The inherent data richness, combined with the undersampling of solution snapshots and truncation of the constructed basis, provides enough grounds to forgo further parameterization.

4.2.1. Problem setup and discretization

The Ahmed body geometry consists of an extruded rectangular shape with a rounded nose at the front and a downward-slanted rear surface (Figure 5). In the configuration considered here, the slant angle is set to 20° . The fluid flow is modeled as compressible air, with a free-stream velocity of $v_\infty = 60$ m/s and a zero-degree angle of attack. Air is treated as a perfect gas. The corresponding Reynolds number based on the body length is $Re = 4.29 \times 10^6$. DES is employed to simulate the flow around this instance of the Ahmed body, utilizing Reichardt’s law of the wall to model boundary layers. The plane of symmetry is utilized to halve the computational domain, while adiabatic wall boundary conditions are imposed on the body’s surface. The outflow boundary is placed far enough downstream to prevent wake contamination (see Figure 5).

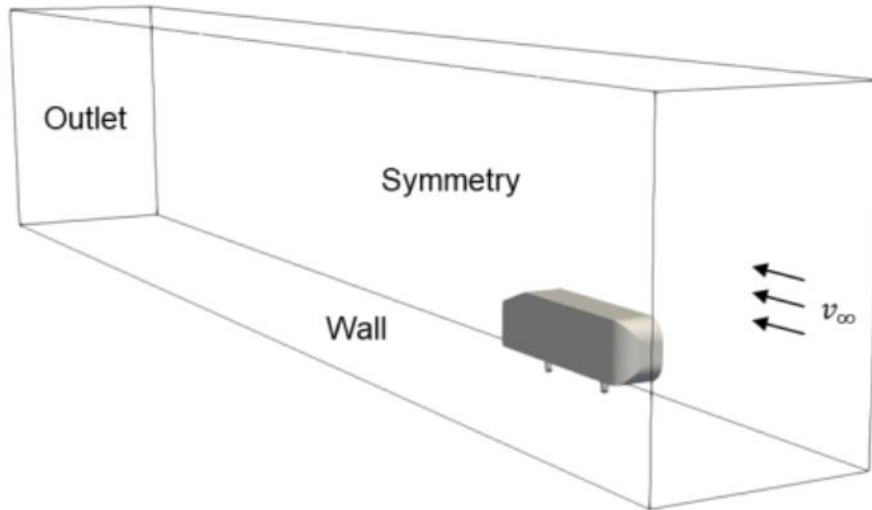


Figure 5: Ahmed body turbulent wake flow problem: computational fluid domain.

The half-domain is discretized using an *unstructured* tetrahedral mesh, following the meshing strategies outlined in [6, 16]. Each vertex in the mesh has $d_e = 6$ unknowns, with a total of $N_v = 2\,890\,434$ vertices and $N_e = 17\,017\,090$ tetrahedra, leading to a state-space dimension of $N = d_e \times N_v = 17\,342\,604$.

The DES equations are time-integrated using a second-order, three-point backward difference scheme with a fixed time step of $\Delta t = 8 \times 10^{-5}$ s. The HDM-based simulation proceeds until a final time of $T_f = 0.2$ s, requiring 2500 time steps. At each step, the resulting nonlinear system of algebraic equations is solved using a Newton-Krylov method combined with an additive Schwarz preconditioned GMRES solver [34] for handling the linear subproblems.

All simulations utilize double-precision arithmetic and are executed on the previously described Linux cluster. The HDM-based simulation, running on 240 cores of this cluster, takes approximately 10 hours of wall-clock time to complete.

4.2.2. Construction, training, and partitioning of the reduced-order basis and nonlinear maps

Unsteady solution snapshots from the HDM model are collected every $2\Delta t$ over the time interval $t \in [0, 0.2]$ seconds, resulting in a total of $N_s = 1251$ solution snapshots. The snapshot matrix $\mathbf{S} \in \mathbb{R}^{N \times N_s}$ is constructed, and a thin SVD is performed to extract a ROB partitioned as $[\mathbf{V}, \bar{\mathbf{V}}]$. The total number of POD modes, $n + \bar{n}$, is chosen to capture at least 99.99% of the singular value energy, leading to $n + \bar{n} = 636$.

For the nonlinear PROMs, the number of retained modes is set to $n = 39$, resulting in $\bar{n} = 597$ discarded modes. This choice follows [16], where a heuristic procedure in the construction of the quadratic PROM (QPROM) for the same Ahmed body turbulent wake problem led to $n = 39$. This provides a natural reference point for direct comparisons between the nonlinear PROMs with closure modeling in the latent space and the QPROM developed in [16].

While this study explores additional configurations with progressively reduced primary basis dimensions n specifically for PROM-RBF, it does not do so for PROM-ANN and PROM-GPR. This decision is based on three reasons: first, a similar study for PROM-ANN was conducted in [18] for the Burgers IBVP (31); second, PROM-GPR and PROM-RBF are implementation variants of the same modeling approach; and third, limitations on space prevent a comprehensive exploration of all three models. The examined configurations for PROM-RBF include $(n, \bar{n}) = (39, 597)$, $(10, 626)$, and $(5, 631)$.

The construction and training of nonlinear closure maps for the PROM-ANN, PROM-GPR, and PROM-RBF models follow the methodology outlined for the Burgers IBVP discussed in Section 4.1. Each nonlinear map $\mathcal{N}(\cdot) : \mathbb{R}^n \rightarrow \mathbb{R}^{\bar{n}}$ is trained on pairs $(\mathbf{q}, \bar{\mathbf{q}})$ derived from the collected solution snapshots, where $\mathbf{q} \in \mathbb{R}^n$ and $\bar{\mathbf{q}} \in \mathbb{R}^{\bar{n}}$. For each model, the training methodology and hyperparameters – such as the number and size of layers for the ANN, as well as the kernel, length scale, noise, and regularization bounds for the RBF and GPR models – are specified and discussed below. In all cases, 90% of the solution snapshots are allocated to training, while 10% are reserved for validation.

For the ANN closure, extensive testing was conducted across multiple architectures, varying both depth (number of layers) and width (number of neurons per layer). These tests consistently indicated that shallow but wide neural networks generally outperform deeper architectures in this setting. Again, this is likely due to the limited size of the training dataset, which favors fewer layers to avoid overfitting and promote more stable training. Consequently, a shallow network comprising a single hidden layer with 4096 neurons and ELU activation is selected, offering the best balance between accuracy and architectural complexity.

A GPR closure is constructed using a Matérn kernel with a smoothness parameter $\nu = 1.5$, combined with a constant term bounded between 10^{-3} and 10^2 , and an initial length scale ℓ set to 1.0 with bounds of 10^{-1} to 2. Maximum log-likelihood optimization is performed using the L-BFGS-B optimizer from the `scikit-learn` library, resulting in an optimized constant-kernel value of 0.11 and a Matérn-kernel length scale of $\ell = 0.46$.

For the RBF closure, a straightforward grid search is employed to demonstrate the simplicity and computational efficiency of training RBF models. The kernel type and shape parameter (ϵ) are optimized through a grid search spanning the range $[0.2, 5]$, discretized into 100 logarithmically spaced points, while the regularization parameter is fixed at $\lambda = 10^{-8}$. Only Gaussian and inverse multiquadric kernels are considered for this grid search, with the inverse multiquadric kernel consistently yielding the best results. For the configuration $(n, \bar{n}) = (39, 597)$, the optimal shape parameter is determined to be $\epsilon = 0.24$.

The RBF closure trained in only 2.1 minutes, compared to 30.0 minutes for the GPR, and 50.7 minutes for ANN, highlighting the efficiency of the simple grid-search strategy selected for the RBF. While the gradient based optimization of the marginal likelihood chosen for the GPR is more expensive in this case, it is important to note that this is problem and optimizer dependent, and the hyperparameters of GPR could also be optimized using a grid search and cross-validation, with a squared error loss function such as that used for the RBF or a probability based loss function leveraging the probabilistic framework.

Furthermore, additional RBF models are trained with progressively smaller n , specifically $(n, \bar{n}) = (10, 626)$ and $(5, 631)$, resulting in optimal shape parameters of approximately $\epsilon = 2.08$ and $\epsilon = 4.54$, respectively, and with training times reduced to only 0.75 and 0.50 minutes. The corresponding results are summarized in Table 4.

4.2.3. Hyperreduction using the ECSW method

As with the Burgers IBVP discussed in Section 4.1, ECSW is employed to hyperreduce each constructed reduced-order model by training it on projected residuals while maintaining a consistent training tolerance

Computational model	n	\bar{n}	n_e	Mesh support elements	Wall-clock time (min)
HPROM (ECSW)	636	-	7 467	761 053	532.51
HPROM-ANN (ANN)	39	597	-	-	50.69
HPROM-ANN (ECSW)	39	597	629	108 519	32.12
HPROM-GPR (GPR)	39	597	-	-	30.02
HPROM-GPR (ECSW)	39	597	496	88 238	23.56
HPROM-RBF (RBF)	39	597	-	-	2.14
HPROM-RBF (ECSW)	39	597	535	84 092	37.88
HPROM-RBF (RBF)	10	626	-	-	0.75
HPROM-RBF (ECSW)	10	626	136	21 380	16.12
HPROM-RBF (RBF)	5	631	-	-	0.50
HPROM-RBF (ECSW)	5	631	72	12 222	12.65

Table 4: Offline computational timings for the Ahmed body turbulent wake flow problem: ECSW computations are performed on 240 CPU cores; the nonlinear closures ANN, GPR, and RBF are trained on 24 cores.

of $\varepsilon_{\text{ECSW}} = 10^{-2}$. In all cases, ECSW training utilizes every 45th snapshot from the collected solution trajectories. The characteristics of the resulting reduced meshes are reported in Table 4.

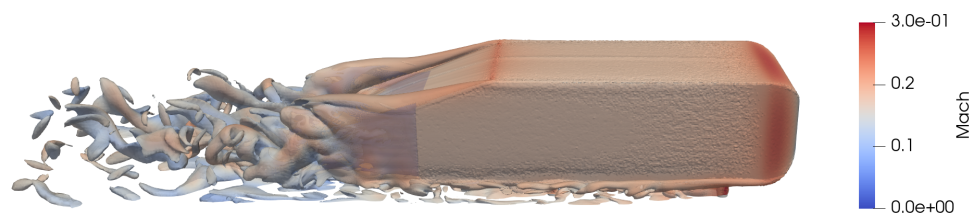
For the traditional HPROM, ECSW identifies a relatively large reduced mesh comprising 7 467 elements, which, along with adjacent elements required by the FV stencil, results in a total mesh support of 761 053 elements (approximately 4.47% of the number of elements of the full CFD mesh). In contrast, ECSW produces significantly smaller reduced meshes for the nonlinear PROMs: 629 elements with a total mesh support of 108 519 elements (0.64%) for HPROM-ANN; 496 elements, yielding a total mesh support of 88 238 elements (0.52%), for HPROM-GPR with $(n, \bar{n}) = (39, 597)$; 535 elements, resulting in a total mesh support of 84 092 elements (0.49%), for HPROM-RBF with $(n, \bar{n}) = (39, 597)$; 136 elements with a total mesh support of 21 380 elements (0.13%) for HPROM-RBF with $(n, \bar{n}) = (10, 626)$; and just 72 elements, leading to a total mesh support of 12 222 elements (0.07%), for HPROM-RBF with $(n, \bar{n}) = (5, 631)$. This progressive reduction demonstrates the direct correlation between the number of retained modes and the size of the ECSW-constructed reduced mesh.

The wall-clock timings in Table 4 indicate that all training costs are reasonable, both in absolute terms and relative to the cost of a single HDM simulation. Particularly, training the nonlinear closure map for PROM-RBF is exceptionally quick.

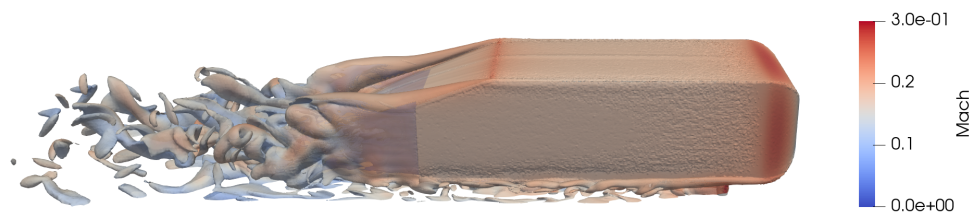
4.2.4. Performance comparisons

The hyperreduced counterparts of the traditional PROM, along with the ANN-, GPR-, and RBF-based nonlinear PROMs, are compared here in terms of their accuracy and performance relative to HDM.

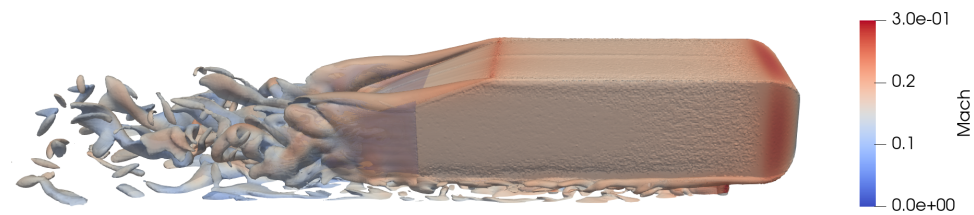
Figure 6 displays iso-vorticity contours for the HDM, HPROM, HPROM-ANN, HPROM-GPR, and HPROM-RBF models, with the parameters $(n, \bar{n}) = (39, 597)$ at $t = 0.2$ seconds. Additional visuals for lower-dimensional RBF variants are omitted for brevity. This figure demonstrates that each method effectively reproduces the unsteady separation and reattachment within the wake region, with the resulting flow structures closely matching those of the HDM reference.



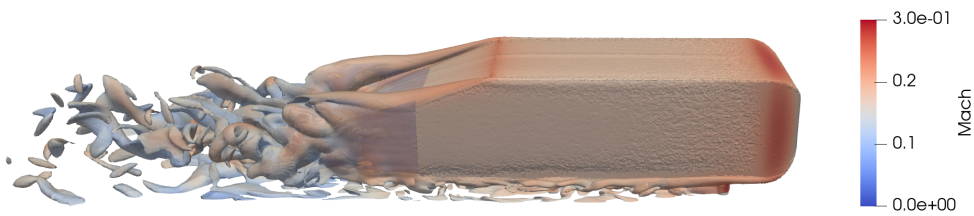
(a) HDM



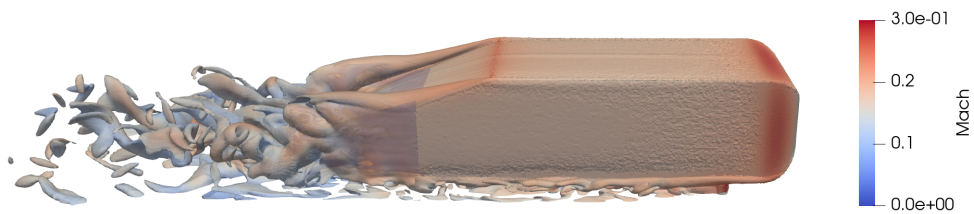
(b) HPROM ($n = 636$)



(c) HPROM-ANN ($n = 39$, $\bar{n} = 597$)



(d) HPROM-GPR ($n = 39$, $\bar{n} = 597$)



(e) HPROM-RBF ($n = 39$, $\bar{n} = 597$)

Figure 6: Ahmed body turbulent wake flow problem: iso-vorticity contours colored by the local Mach number and computed at $t = 2 \times 10^{-1}$ s, using various computational models.

Figures 7 and 8 show the time histories of the drag coefficient C_D , lift coefficient C_L , and the scaled velocity components u_x/v_∞ and u_z/v_∞ at a probe in the body’s wake, computed using both HDM and all hyperreduced counterparts. Although the predictions appear qualitatively similar, the standard Euclidean norm can penalize minor phase discrepancies. To better evaluate the effects of these discrepancies on overall accuracy, Table 5 includes errors for the aforementioned QoIs, computed using the dynamic time warping (DTW) distance [35]. Specifically, these errors are assessed here as follows

$$\mathbb{RE}_{\text{DTW}, \text{QoI}} = \frac{\text{DTW} \left(\text{QoI}(t), \widetilde{\text{QoI}}(t) \right)}{\sqrt{\sum_{m=0}^{N_t} \|\text{QoI}^m\|_2^2}}$$

For $(n, \bar{n}) = (39, 597)$, HPROM-ANN, HPROM-RBF, and HPROM-GPR deliver broadly similar accuracy across most error metrics. Interestingly, HPROM-RBF shows slightly lower Euclidean norm errors for the flow variables, whereas HPROM-GPR demonstrates marginal advantages in DTW-based errors.

Computational model	n	\bar{n}	\mathbb{RE}_{2, C_D} (%)	\mathbb{RE}_{2, C_L} (%)	\mathbb{RE}_{2, u_x} (%)	\mathbb{RE}_{2, u_z} (%)	$\mathbb{RE}_{\text{DTW}, C_D}$ (%)	$\mathbb{RE}_{\text{DTW}, C_L}$ (%)	$\mathbb{RE}_{\text{DTW}, u_x}$ (%)	$\mathbb{RE}_{\text{DTW}, u_z}$ (%)
HDM	17 342 604	-	-	-	-	-	-	-	-	-
HPROM	636	-	0.39	2.64	1.36	7.96	0.08	0.48	0.25	1.43
HPROM-ANN	39	597	0.37	2.44	1.35	7.17	0.09	0.57	0.26	1.44
HPROM-GPR	39	597	0.38	2.79	1.42	7.90	0.09	0.29	0.11	0.77
HPROM-RBF	39	597	0.21	1.52	0.80	4.42	0.06	0.46	0.15	0.85
HPROM-RBF	10	626	0.58	5.00	2.10	12.03	0.07	0.51	0.22	1.41
HPROM-RBF	5	631	0.79	6.21	2.99	17.74	0.10	0.53	0.20	2.50

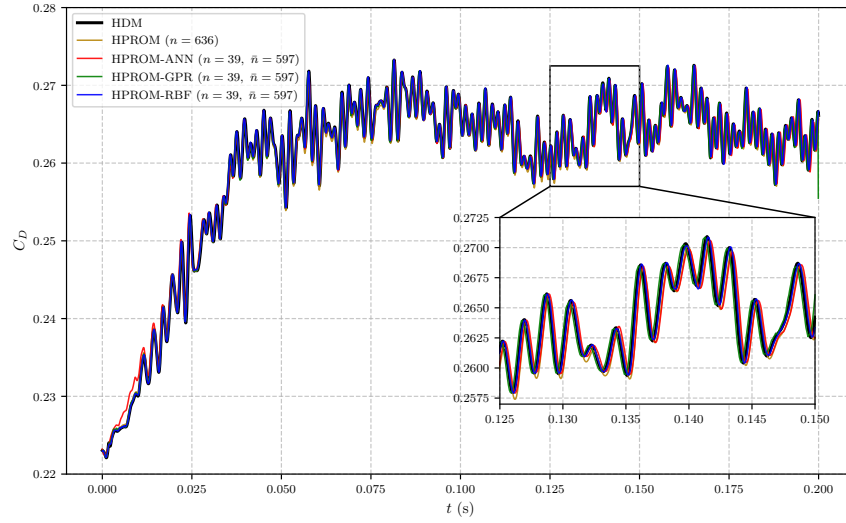
Table 5: Ahmed body turbulent wake flow problem: relative errors in the Euclidean norm and DTW distance for global quantities (C_D , C_L) and local quantities at wake probes (normalized velocities).

Table 6 presents the online computational performance for each model, highlighting wall-clock times and speedups relative to the HDM model, which runs on 240 cores. All HPROMs are executed on 8 cores. The column labeled $\mathbb{RE}_{\text{DTW}, \text{QoI}}^{\max}$ displays the maximum DTW-based error among the four QoIs: C_D , C_L , u_x , and u_z , as listed in Table 5. Reducing n , as done for HPROM-RBF, can significantly enhance speedup while maintaining high accuracy in DTW metrics.

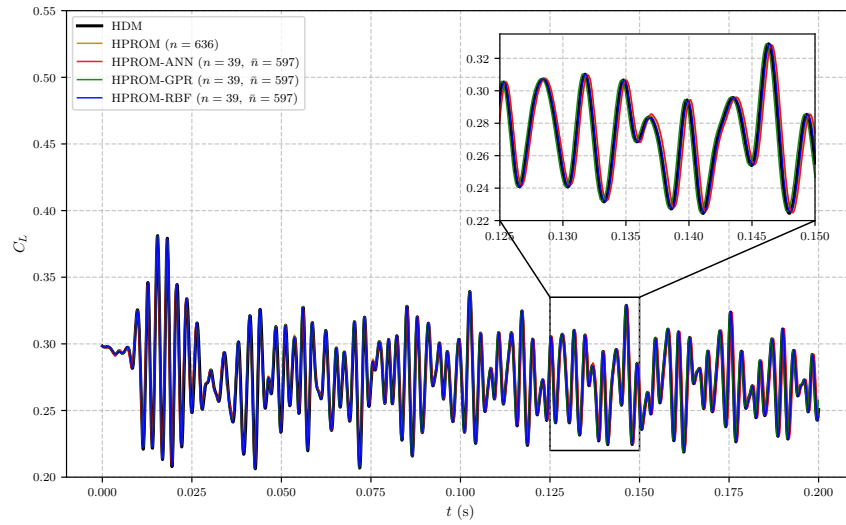
Computational model	n	\bar{n}	n_e	$\mathbb{RE}_{\text{DTW}, \text{QoI}}^{\max}$ (%)	Wall-clock time (min)	Speedup (wall)	Speedup (CPU)
HDM	17 342 604	-	17 017 090	-	611.94	-	-
HPROM	636	-	7 467	1.43	129.02	4.74	142.29
HPROM-ANN	39	597	629	1.44	12.20	50.15	1 504.42
HPROM-GPR	39	597	496	0.77	9.53	64.18	1 925.41
HPROM-RBF	39	597	535	0.85	9.51	64.35	1 930.61
HPROM-RBF	10	626	136	1.41	3.12	196.38	5 891.26
HPROM-RBF	5	631	72	2.50	1.84	333.15	9 994.46

Table 6: Ahmed body turbulent wake flow problem: online performance comparison (computational speedups) of traditional and nonlinear HPROMs (HDM is processed on 240 cores and all HPROMs are run on 8 cores).

As demonstrated in Table 6, HPROM-ANN, HPROM-GPR, and HPROM-RBF achieve significantly greater speedups compared to the traditional HPROM model, while maintaining equal or superior accuracy. Specifically, for $(n, \bar{n}) = (39, 57)$, HPROM-GPR and HPROM-RBF attain speedups and accuracy levels akin to those of the hyperreduced QPROM (HQPROM) model for this Ahmed body turbulent wake flow problem, as reported in [16], while also enabling further reductions in n (down to 10 and 5 for PROM-RBF) with good accuracy. However, for PROM-ANN, ECSW selects a slightly larger reduced mesh than for PROM-GPR and PROM-RBF, resulting in a modest decrease in speedup for HPROM-ANN. This outcome is influenced by the problem setup and ANN hyperparameters (e.g., architecture, activation functions), underscoring the advantage of employing multiple closure strategies when designing a nonlinear HPROM.

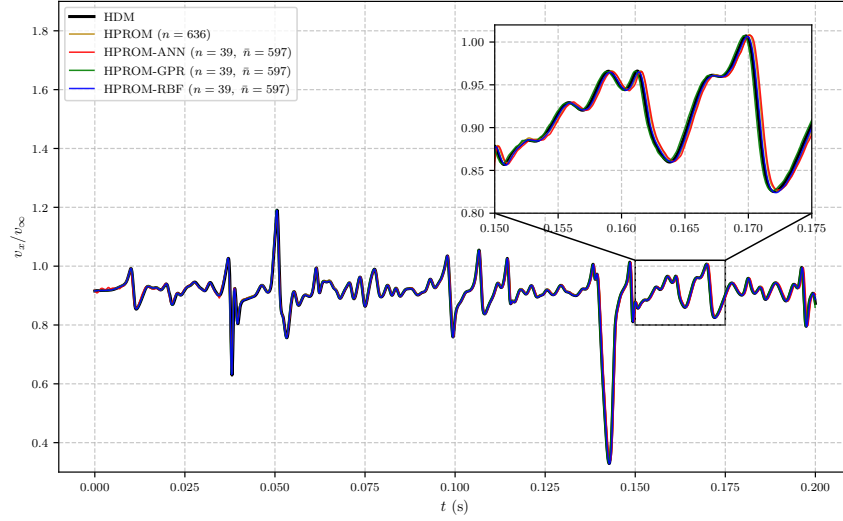


(a) Time history of C_D .

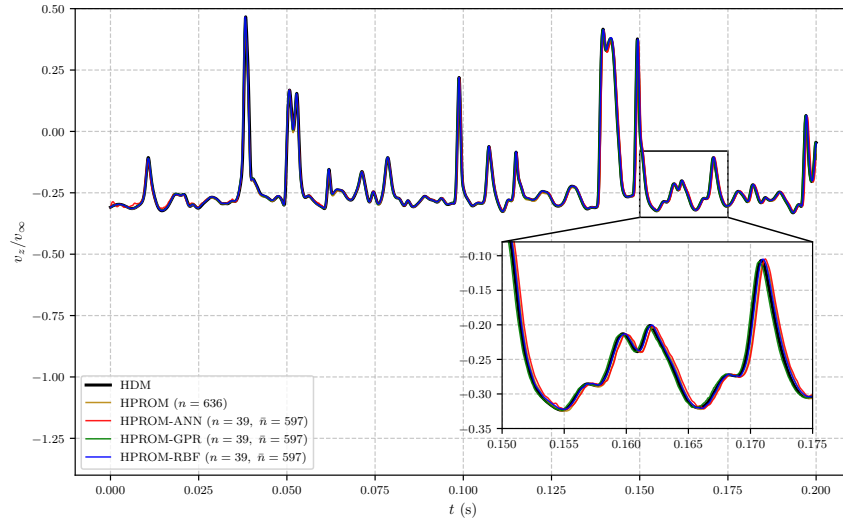


(b) Time-history of C_L .

Figure 7: Ahmed body turbulent wake flow problem: time histories of the drag coefficient C_D (a) and lift coefficient C_L (b), predicted using various computational models.



(a) Time-history of v_x/v_∞ at a probe.



(b) Time-history of v_z/v_∞ at a probe.

Figure 8: Ahmed body turbulent wake flow problem: time-histories of the streamwise velocity v_x/v_∞ (a) and vertical velocity v_z/v_∞ (b), predicted using various computational models.

5. Conclusions

This work advances nonlinear projection-based model order reduction (PMOR) by addressing closure error in the latent space through two alternative approaches: Gaussian process regression (GPR) and radial basis function (RBF) interpolation. Building on the framework established in [18, 4], which enhances PMOR using artificial neural networks (ANNs), these new strategies incorporate either GPR or RBF closures. They retain the key advantage of the ANN-based projection-based reduced-order model (PROM-ANN): computational complexity is independent of the problem’s high dimension N , scaling only with the smaller latent dimensions n and \bar{n} . All three closures—based on ANN, GPR, or RBF integrate seamlessly with existing hyperreduction techniques, which are essential for many large-scale applications.

Numerical experiments on the two-dimensional parametric inviscid Burgers problem and the industrial-scale Ahmed body turbulent wake flow demonstrate the effectiveness of these closure techniques. For the Burgers problem, the hyperreduced models HPROM-GPR and HPROM-RBF achieve speedups of approximately 43–47 times while maintaining an accuracy above 98%, with dimensions smaller than those of the traditional HPROM. In this case, HPROM-ANN attains a similar speedup of around 43 times with comparable accuracy.

For the Ahmed body flow, both GPR and RBF closures provide robust predictions and substantial speedups, reaching up to 64 times in wall-clock time and 1930 times CPU speedup at $(n, \bar{n}) = (39, 597)$. Notably, at a reduced dimension of $(n, \bar{n}) = (5, 631)$, HPROM-RBF achieves a wall-clock time speedup of 333 times and a CPU speedup of 9990 times, with only a 2.5% error margin. In comparison, HPROM-ANN provides a wall-clock speedup of 50 times and a CPU speedup of 1504 times.

Therefore, for both problems, HPROM-GPR and HPROM-RBF are as fast or faster than HPROM-ANN and achieve comparable, if not superior, accuracy.

GPR- and RBF-based closures stand out through their interpretability. While ANNs offer expressive representations capable of capturing complex relationships with abundant training data, GPRs provide explicit formulations that enable automatic hyperparameter tuning, and RBFs excel in deterministic evaluations, particularly when data availability is moderate.

Another practical advantage is that both GPR- and RBF-based closures require significantly less training data, avoiding the need to generate additional samples beyond the initial high-dimensional solution snapshots.

In terms of training efficiency, GPR closures – which leverage probabilistic hyperparameter optimization – required in our study significantly longer training times than RBF interpolation trained via cross-validation coupled with adaptive or non-adaptive search algorithms (for the Burgers problem, 96.1 minutes for GPR vs. 13.2 minutes for RBF; for the Ahmed body, 30.0 minutes for GPR vs. 2.1 minutes for RBF). While this difference is likely problem dependent, and similar training algorithms could be applied to both closures, it underscores the value of retaining both probabilistic and deterministic viewpoints.

Finally, although in this study the online predictions of GPR closures were evaluated using the posterior mean only – since the predictive variance does not influence the reduced solve but would add to the online cost – predictive variance remains a distinctive strength of GPR. It offers a promising avenue for future work on adaptive sampling and error indicators.

Regarding hyperreduction, ECSW-based reduced mesh selection maintains consistent mesh sizes across different closure strategies, although problem-specific factors can introduce some variations, as seen in the Ahmed body case. This diversity of closure approaches enhances the framework’s adaptability to specific problem requirements.

In summary, PROM-GPR and PROM-RBF significantly broaden the scope of nonlinear PMOR, providing notable benefits in efficiency, accuracy, and interpretability. They exhibit strong potential for handling shock-dominated parametric flows and complex turbulent flows, effectively mitigating the Kolmogorov barrier. Future research will focus on selecting optimal latent dimensions and integrating these methodologies with piecewise-affine local bases [5, 6], further enhancing robustness and efficiency in realistic, nonlinear engineering contexts.

Acknowledgments

Charbel Farhat and Radek Tezaur acknowledge partial support by the Office of Naval Research under Grant N00014-23-1-2877 and Grant N00014-23-1-2413; and partial support by the Air Force Office of Scientific Research under Grant FA9550-22-1-0004 and Grant FA9550-20-1-0358.

Sebastian Ares de Parga acknowledges partial support by the Departament de Recerca i Universitats de la Generalitat de Catalunya under Grant FI-SDUR 2021; partial support by the Fulbright Commission Spain through a Fulbright Predoctoral Research Fellowship (2024–2025); and partial support by the Department of Aeronautics and Astronautics at Stanford University.

References

- [1] Athanasios C Antoulas. *Approximation of large-scale dynamical systems*. SIAM, 2005.
- [2] Alfio Quarteroni, Gianluigi Rozza, et al. *Reduced order methods for modeling and computational reduction*, volume 9. Springer, 2014.
- [3] Wanli He, Philip Avery, and Charbel Farhat. In situ adaptive reduction of nonlinear multiscale structural dynamics models. *International Journal for Numerical Methods in Engineering*, 121(22):4971–4988, 2020.
- [4] Matthew R Chmiel, Joshua Barnett, and Charbel Farhat. Unified LSPG model reduction framework and assessment for hypersonic computational fluid dynamics. *AIAA Journal*, 63(1):72–90, 2025.
- [5] David Amsallem, Matthew J Zahr, and Charbel Farhat. Nonlinear model order reduction based on local reduced-order bases. *International Journal for Numerical Methods in Engineering*, 92(10):891–916, 2012.
- [6] Sebastian Grimberg, Charbel Farhat, Radek Tezaur, and Charbel Bou-Mosleh. Mesh sampling and weighting for the hyperreduction of nonlinear Petrov–Galerkin reduced-order models with local reduced-order bases. *International Journal for Numerical Methods in Engineering*, 122(7):1846–1874, 2021.
- [7] Melissa B Rivers and Ashley Dittberner. Experimental investigations of the nasa common research model. *Journal of Aircraft*, 51(4):1183–1193, 2014.
- [8] Kevin Carlberg, Charbel Bou-Mosleh, and Charbel Farhat. Efficient non-linear model reduction via a least-squares Petrov–Galerkin projection and compressive tensor approximations. *International Journal for Numerical Methods in Engineering*, 86(2):155–181, 2011.
- [9] Kevin Carlberg, Charbel Farhat, Julien Cortial, and David Amsallem. The GNAT method for non-linear model reduction: effective implementation and application to computational fluid dynamics and turbulent flows. *Journal of Computational Physics*, 242:623–647, 2013.
- [10] Kyle M Washabaugh, Matthew J Zahr, and Charbel Farhat. On the use of discrete nonlinear reduced-order models for the prediction of steady-state flows past parametrically deformed complex geometries. In *54th AIAA Aerospace Sciences Meeting*, page 1814, 2016.
- [11] Tommaso Taddei. A registration method for model order reduction: data compression and geometry reduction. *SIAM Journal on Scientific Computing*, 42(2):A997–A1027, 2020.
- [12] Marzieh Alireza Mirhoseini and Matthew J Zahr. Model reduction of convection-dominated partial differential equations via optimization-based implicit feature tracking. *Journal of Computational Physics*, page 111739, 2022.
- [13] Tommaso Taddei and Lei Zhang. Registration-based model reduction in complex two-dimensional geometries. *Journal of Scientific Computing*, 88:1–25, 2021.
- [14] Victor Zucatti and Matthew J Zahr. Model reduction of convection-dominated viscous conservation laws using implicit feature tracking and landmark image registration. *arXiv preprint arXiv:2503.17463*, 2025.
- [15] Shobhit Jain, Paolo Tiso, Johannes B Rutzmoser, and Daniel J Rixen. A quadratic manifold for model order reduction of nonlinear structural dynamics. *Computers & Structures*, 188:80–94, 2017.

- [16] Joshua Barnett and Charbel Farhat. Quadratic approximation manifold for mitigating the Kolmogorov barrier in nonlinear projection-based model order reduction. *Journal of Computational Physics*, 464:111348, 2022.
- [17] Boris Kramer, Benjamin Peherstorfer, and Karen E Willcox. Learning nonlinear reduced models from data with operator inference. *Annual Review of Fluid Mechanics*, 56(1):521–548, 2024.
- [18] Joshua Barnett, Charbel Farhat, and Yvon Maday. Neural-network-augmented projection-based model order reduction for mitigating the Kolmogorov barrier to reducibility. *Journal of Computational Physics*, 492:112420, 2023.
- [19] Albert Cohen, Charbel Farhat, Yvon Maday, and Agustin Somacal. Nonlinear compressive reduced basis approximation for PDEs. *Comptes Rendus. Mécanique*, 351(S1):357–374, 2023.
- [20] Chris Homescu, Linda R Petzold, and Radu Serban. Error estimation for reduced-order models of dynamical systems. *SIAM Journal on Numerical Analysis*, 43(4):1693–1714, 2005.
- [21] John R Singler. New POD error expressions, error bounds, and asymptotic results for reduced order models of parabolic PDEs. *SIAM Journal on Numerical Analysis*, 52(2):852–876, 2014.
- [22] Charbel Farhat, Philip Avery, Todd Chapman, and Julien Cortial. Dimensional reduction of nonlinear finite element dynamic models with finite rotations and energy-based mesh sampling and weighting for computational efficiency. *International Journal for Numerical Methods in Engineering*, 98(9):625–662, 2014.
- [23] Charbel Farhat, Todd Chapman, and Philip Avery. Structure-preserving, stability, and accuracy properties of the energy-conserving sampling and weighting method for the hyper reduction of nonlinear finite element dynamic models. *International Journal for Numerical Methods in Engineering*, 102(5):1077–1110, 2015.
- [24] Noel Cressie. The origins of kriging. *Mathematical Geology*, 22:239–252, 1990.
- [25] Carl Edward Rasmussen. Gaussian processes in machine learning. In *Summer school on machine learning*, pages 63–71. Springer, 2003.
- [26] Robert B Gramacy. *Surrogates: Gaussian Process Modeling, Design, and Optimization for the Applied Sciences*. Chapman and Hall/CRC, 2020.
- [27] Martin Dietrich Buhmann. Radial basis functions. *Acta Numerica*, pages 1–38, 2000.
- [28] Charbel Farhat, Philippe Geuzaine, and Gregory Brown. Application of a three-field nonlinear fluid–structure formulation to the prediction of the aeroelastic parameters of an F-16 fighter. *Computers & Fluids*, 32(1):3–29, 2003.
- [29] Eli Turkel. Preconditioning techniques in computational fluid dynamics. *Annual Review of Fluid Mechanics*, 31(1):385–416, 1999.
- [30] Victor M Panaretos and Yoav Zemel. Statistical aspects of wasserstein distances. *Annual Review of Statistics and Its Application*, 6(1):405–431, 2019.
- [31] Marie Jose Azzi and Charbel Farhat. Enhanced multimodal nonparametric probabilistic method for model-form uncertainty quantification and digital twinning. *AIAA Journal*, 62(11):4265–4279, 2024.
- [32] Meinard Müller. Dynamic time warping. *Information retrieval for music and motion*, pages 69–84, 2007.
- [33] Syed R Ahmed, G Ramm, and Gunter Faltn. Some salient features of the time-averaged ground vehicle wake. *SAE transactions*, pages 473–503, 1984.
- [34] Xiao-Chuan Cai, Charbel Farhat, and Marcus Sarkis. A minimum overlap restricted additive schwarz preconditioner and applications in 3d flow simulations. *Contemporary mathematics*, 218:479–485, 1998.

- [35] Tadas Baltrušaitis, Chaitanya Ahuja, and Louis-Philippe Morency. Multimodal machine learning: A survey and taxonomy. *IEEE Transactions on Pattern Analysis and Machine Intelligence*, 41(2):423–443, 2018.